# The Cross-Shelf Regime of a Wind-Driven Supercritical River Plume

# Accepted for publication in Journal of Physical Oceanography

- Elizabeth Yankovsky,<sup>a</sup> Alexander Yankovsky,<sup>b</sup>
- <sup>a</sup> Courant Institute of Mathematical Sciences, New York University, New York, NY, USA
- <sup>5</sup> School of the Earth, Ocean and Environment, University of South Carolina, Columbia, SC, USA

6 Corresponding author: Elizabeth Yankovsky, eyankovsky@gmail.com

ABSTRACT: River plumes are a dominant forcing agent in the coastal ocean, transporting tracers and nutrients offshore and interacting with coastal circulation. In this study we characterize the 8 novel 'cross-shelf' regime of freshwater river plumes. Rather than remaining coastally-trapped 9 (a well-established regime), a wind-driven cross-shelf plume propagates for tens to over one hundred kilometers offshore of the river mouth while remaining coherent. We perform a suite of 11 high-resolution idealized numerical experiments that offer insight into how the cross-shelf regime 12 comes about and the parameter space it occupies. The wind-driven shelf flow comprising the geostrophic along-shelf and the Ekman cross-shelf transport advects the plume momentum and precludes geostrophic adjustment within the plume, leading to continuous generation of internal 15 solitons in the offshore and upstream segment of the plume. The solitons propagate into the plume interior, transporting mass within the plume and suppressing plume widening. We exam-17 ine an additional ultra-high resolution case that resolves submesoscale dynamics. This case is 18 dynamically consistent with the lower resolution simulations, but additionally captures vigorous 19 inertial-symmetric instability leading to frontal erosion and lateral mixing. We support these findings with observations of the Winyah Bay plume, where the cross-shelf regime is observed 21 under analogous forcing conditions to the model. The study offers an in-depth introduction to the cross-shelf plume regime and a look into the submesoscale mixing phenomena arising in estuarine plumes.

SIGNIFICANCE STATEMENT: In this study, we characterize a novel regime of freshwater river plumes. Rather than spreading near to or along the coast, under certain conditions river plumes may propagate away from the coast and remain coherent for tens to over one hundred kilometers offshore. Cross-shelf plumes provide a mechanism by which freshwater and river-borne materials may be transported into the open ocean, especially across wide continental shelves. Such plumes carry nutrients critical for biological productivity offshore and interact with large-scale oceanic features such as the Gulf Stream. We use high-resolution numerical modeling to examine how the cross-shelf regime arises, and support our findings with observational evidence. We also study the mixing phenomena and fluid instabilities evolving within such plumes.

A salient feature of the coastal ocean is that cross-shelf gradients of pressure and density are

### 1. Introduction

35

an order of magnitude (or more) higher than the corresponding along-shelf gradients, which, 36 through geostrophic adjustment, results in predominantly along-shelf circulation and transport (Brink 2016). This highly polarized pressure and density distribution is disrupted by localized sources of brackish water running off from estuary or river mouths. The resulting density anomaly frequently reaches  $O(10 \text{ kg m}^{-3})$  (Yankovsky et al. 2022), a buoyancy forcing magnitude seldom seen in the open ocean. The buoyant outflow tends to spread radially in the form of a gravity 41 current from its source (at least when unopposed by the ambient shelf circulation, e.g., O'Donnell 42 (1990)), forming a nearly circular coastal buoyant plume (Garvine 1984). The complex dynamics associated with the advancing front of the buoyant plume are reviewed by O'Donnell (2010), while an example of modern observations of frontal processes can be found in Delatolas et al. (2023). The periphery of the plume reaches a geostrophic, or sometimes a gradient wind balance (Yankovsky and Chapman 1997), resulting in an anticyclonic flow pattern commonly referred to as an anticyclonic bulge. 48 There is a tendency for the anticyclonic bulge to grow indefinitely (Nof and Pichevin 2001). 49 However, this tendency breaks down due to the development of various instabilities (e.g., Oey and

Mellor (1993); Jia and Yankovsky (2012); Izett and Fennel (2018)). The excessive buoyant water is

transported downstream so that the anticyclonic bulge approaches a spatial limit, albeit fluctuating

with time. Sharples et al. (2017) related the spatial scale of the anticyclonic bulge to the shelf

width as a metric for the delivery of riverine nutrients across the shelf break, a process of primary importance for deep-ocean ecosystems.

The buoyant flow ultimately exits the anticyclonic bulge and evolves into a coastally-trapped buoyant current propagating alongshore in the direction of Kelvin wave phase (hereinafter referred to as downstream) and exhibiting a geostrophic balance in the cross-shelf direction. This natural downstream propagation can be reversed under the influence of wind forcing or deep ocean circulation impinging on the shelf. The wind-induced reversal of the buoyant coastal current is associated with upwelling conditions, such that the buoyant water propagates not only upstream, but also offshore, in the surface boundary layer. The offshore transport is sustained by Ekman dynamics. Regardless of the direction (downstream vs. upstream), both patterns typically reveal significant alongshore extension of buoyant water which retains its contact with the coastline (e.g., Hickey et al. (2009)).

This study addresses a less frequent regime, where the plume detaches from the coast near the mouth and crosses the shelf at an oblique angle as an elongated tongue of buoyant water. This regime was described and referred to as a cross-shelf plume in the recent observational study of the Winyah Bay plume off the South Carolina coast, USA, by Yankovsky et al. (2022), where similar plumes at other locations were also briefly discussed. The important finding of Yankovsky et al. (2022) is that cross-shelf plumes are formed under the influence of light to moderate upwelling-favorable wind, and the buoyant layer remains supercritical in terms of the internal Froude number tens of km away from the source (an estuary mouth). Froude number is defined as:

$$F = U_s/C_i, (1)$$

where  $U_s$  is near-surface velocity magnitude typically averaged over the buoyant layer depth, and  $C_i$  is internal gravity wave phase speed. The supercriticality is maintained by superposition of the inherent flow field associated with the plume density anomaly (which tends to achieve a geostrophic balance) and the wind-induced Ekman drift. Yankovsky et al. (2022) assessed supercriticality by solving an internal wave (IW) eigenvalue problem and recovering the gravest IW mode dispersion curve for an arbitrary buoyancy frequency profile and a vertically sheared mean current. This is a more accurate approach than a slab-like representation of a buoyant layer typically utilized for

- internal Froude number estimates (e.g., Branch et al. (2020), Geyer and Ralston (2011), Hetland (2010), MacDonald and Geyer (2005), among many others).
- Supercritical buoyant outflows are frequent in nature, and can be identified by a liftoff, or detachment from the bottom, of a buoyant layer near the mouth, where an internal hydraulic jump occurs. Such outflows are also characterized by high Burger number (Bu) at the mouth, where Bu is the ratio of the baroclinic Rossby radius to the mouth width:

$$Bu = \sqrt{g'h}/(fW). \tag{2}$$

Here  $g' = |g\Delta\rho|/\rho_0$  is the reduced gravity, where g is gravitational acceleration,  $\Delta\rho$  is the buoyant layer density anomaly relative to the ambient seawater of density  $\rho_0$ , h is the buoyant layer thickness, f is the Coriolis parameter, and W is the mouth width. The significance of the supercritical regime in the plume near field (as defined by Garvine (1984); see also Horner-Devine et al. (2015)) was discussed mostly in terms of the buoyant layer mixing and entrainment (Hetland 2005, 2010). In 91 fact, the internal Froude number can be related to the Richardson number (O'Donnell 1990), with 92 the latter governing Kelvin-Helmholtz instability, and consequently the mixing and entrainment across the interface of the buoyant layer. The role of supercritical flow in setting the plume's spatial structure has seldom been addressed. The notable exceptions are a series of papers by Garvine 95 (1984, 1987) and O'Donnell (1990), as well as some references therein. In these studies, the plume 96 structure is determined by propagation properties of internal waves (expressed mathematically as characteristic lines in a corresponding solution) which lead to the formation of trailing fronts and 98 interior jumps within the plume, also referred to as interior fronts. Under unforced conditions, the plume cannot remain supercritical over long distances from the mouth due to rapid momentum dissipation, but superimposed light wind stress can change this situation (Yankovsky et al. 2022). 101 In this study, we address the formation of the cross-shelf plume by means of idealized numerical 102 modeling. As demonstrated by Yankovsky et al. (2022), the cross-shelf plume does not exhibit substantial transverse (lateral) spreading which implies some inherent dynamics sustaining the 104 coherent plume structure. A set of numerical experiments retaining the essential ingredients of a 105 cross-shelf plume is intended to delineate these dynamics. The rest of the paper is organized as 106 follows: Section 2 describes the model configuration and governing parameters. Section 3 presents the model results beginning with a coastally-trapped plume and then examining the emergence,

properties, and parameter space of the cross-shelf plume regime. Section 4 presents an ultra-high resolution simulation and examines submesoscale mixing dynamics. Section 5 presents satellite observations supporting the model findings, and addresses some inevitable simplifications of the model. Section 6 concludes the paper.

## 2. Numerical model

We use the non-hydrostatic MITgcm (Marshall et al. 1997) to solve the incompressible Boussinesq equations in z-coordinates. The model domain is 3-dimensional and lies on an f-plane, with 115 Coriolis parameter  $f = 8 \cdot 10^{-5} \text{ s}^{-1}$ . A non-linear equation of state is used to solve for density based 116 on McDougall et al. (2003). A Laplacian viscosity with constant horizontal and vertical coefficients  $A_h = 10 \,\mathrm{m^2 \, s^{-1}}$  and  $A_z = 10^{-4} \,\mathrm{m^2 \, s^{-1}}$ , respectively, ensures numerical stability by dissipating energy near the grid scale such that the grid Reynolds number is near order one. Temperature and salinity 119 diffusivities are both set to  $K_h = 10^{-6} \text{ m}^2 \text{ s}^{-1}$  in the horizontal and  $K_z = 10^{-6} \text{ m}^2 \text{ s}^{-1}$  in the vertical. 120 The advection scheme is third-order direct-space-time with a flux limiter. Buoyant outflows with sharp density gradients undergo significant numerical diffusion even when the spatial resolution is 122 relatively high (e.g. Ralston et al. (2017)). For this reason, we apply low diffusivity coefficients in 123 order to prevent excessive erosion of the pycnocline and frontal interfaces, and thus to permit the development of instabilities and internal waves. 125

The zonal and meridional extents of the domain are 60 and 100 km, respectively, and maximum 126 depth is 25 meters. Horizontal grid spacing is dx = 100 m and vertical grid spacing is dz = 0.1 m. A higher-resolution run with dx = 15 m and lower horizontal viscosity ( $A_h = 1.5$  m<sup>2</sup> s<sup>-1</sup>) is also 128 performed as a sensitivity test and to examine smaller-scale dynamical influences. The domain is 129 a periodic meridional channel with zonal open boundary conditions discussed below. The origin of the coordinate system is in the southwestern corner with x, y, and z axes pointing eastward, 131 northward, and upward, respectively, and corresponding velocity components (u, v, w). There is a 132 10 km-wide strip of land along the western boundary, with a coastal wall located at x = 10 km. The 133 land is cut through by a zonal inlet of width W, which is set to 1 km in the standard configuration (W = 5, 10 km are also tested). Buoyant inflow enters the domain through this inlet. The water depth at the coastal wall and within the inlet is 5 m; it linearly increases to 10 m at x = 12 km and 136 then to its maximum value of 25 m at x = 37 km. In one case the alongshore-uniform coastline

is replaced with a coastal promontory (hereinafter, referred to as a cape) similar to the coastline geometry of Winyah Bay. In this case, the coastline linearly recedes to x = 0 km over the 15-km alongshore distance both north and south of the mouth.

The model is forced by a buoyant inflow O specified at the head of the inlet (x = 0 km) with depth-independent inflow velocity. The zonal boundary conditions are such that inflow from the 142 western boundary is balanced by outflow from the eastern boundary. Aside from the inflow, there 143 is no normal flow on the western boundary. The coastal wall uses free slip conditions (zero stress). There is a free surface and the bottom stress is parameterized via quadratic bottom drag with a coefficient of 0.005. The buoyant inflow mimics the buoyancy forcing from Winyah Bay as 146 reported by Yankovsky and Voulgaris (2019) and Yankovsky et al. (2022) and corresponds to the 147 time-averaged riverine freshwater discharge  $Q_r = 800 \text{ m}^3 \text{ s}^{-1}$ . The buoyant inflow is brackish, with 148 the depth-averaged inflow salinity  $\overline{s_i} = 18$ ;  $s_i$  increases linearly from 12 at the surface to 24 at the 149 bottom at x = 0. The ocean ambient salinity is  $s_0 = 34$ . The inflow oscillates with a period of 12.4 150 h (an M2 tidal harmonic). Thus, Q at the inlet head is defined as:

$$Q = Q_r \frac{s_0}{s_0 - \overline{s_i}} [1 + \sin(\omega t)], \tag{3}$$

where t is time and  $\omega$  is the tidal frequency. During the first tidal cycle, no salinity anomaly is prescribed at the inlet head, that is, inflow has the ambient ocean salinity. A constant in time meridional wind stress of 0.03 Pa is applied in the standard model configuration (higher values are also explored). This wind stress direction generates an eastward Ekman transport and leads to upwelling conditions at the western (coastal) boundary.

A total of 11 model runs are reported here (with more sensitivity tests completed) and their configurations are summarized in Table 1. The nominal duration of each model run is 3.1 days (74.4 h), which is 6 full tidal cycle, 5 with buoyancy forcing. However, the model blew up earlier, at  $\sim 2.3$  days in model run SW10 (the strongest wind with standard  $A_z$ ), most likely due to "drying" of the uppermost grid cell. Several diagnostics are used to characterize the model results. The vertical profile of salinity s is reduced to the equivalent freshwater layer thickness:

$$h_f = \int_{-D}^{0} \frac{s_0 - s}{s_0} dz,\tag{4}$$

TABLE 1. Summary of model experiments, with bold text indicating the unique feature of each experiment.

The standard case (S) is listed first. Other abbreviations are: NW = no wind, NT = no tides, M5 = 5 km mouth,

M10 = 10 km mouth, W5 = 0.05 Pa winds, W10 = 0.1 Pa winds, V1 and V2 are alternate viscosity values, HR = high resolution, C = cape geometry.  $R_f$  is defined in Eq. 18 as the fraction of the freshwater volume advected past the channel midpoint at x = 35 km. Values of  $R_f$  are given at two times: (2.3, 3.1) days.

Model Run	Tidal Discharge	W [km]	Coastal Cape	τ [Pa]	$A_z \text{ m}^2 \text{ s}^{-1}$	$\Delta x$ [m]	Bu	$R_f$
S	Yes	1	No	0.03	$10^{-4}$	100	7.31	(0.19, 0.45)
SNW	Yes	1	No	0	$10^{-4}$	100	7.09	(0.0, 0.0)
SNT	No	1	No	0.03	$10^{-4}$	100	7.57	(0.18, 0.44)
SM5	Yes	5	No	0.03	$10^{-4}$	100	1.12	(0.02, 0.29)
SM10	Yes	10	No	0.03	$10^{-4}$	100	0.51	(0.01, 0.25)
SW5	Yes	1	No	0.05	$10^{-4}$	100	7.51	(0.45, 0.61)
SW10	Yes	1	No	0.1	$10^{-4}$	100	7.91	(0.60, N/A)
V1W10	Yes	1	No	0.1	$2\cdot 10^{-4}$	100	8.10	(0.21, 0.37)
V2W10	Yes	1	No	0.1	$10^{-3}$	100	8.74	(0.00, 0.02)
SHR	Yes	1	No	0.03	$10^{-4}$	15	7.87	(N/A, N/A)
SC	Yes	1	Yes	0.03	$10^{-4}$	100	7.55	(0.13, 0.42)

Since the plume occupies only a small fraction of the total water depth D, the internal gravity wave phase speed  $C_i$  is deduced from  $h_f$  as  $C_i = \sqrt{g'h_f}$ , where g' corresponds to the freshwater density anomaly. Burger number (Eq. 2) at the mouth is estimated as Bu =  $C_i/(fW)$ , with  $h_f$  (which varies significantly across the mouth for model runs SM5 and SM10) taking its maximal value across the mouth and averaged over the last tidal cycle. Since there is no stratification in the ambient ocean,  $C_i$  becomes zero there and the internal Froude number becomes infinite. For this reason, we utilize the inverse Froude number:

$$F_i = C_i/U_s. (5)$$

 $U_s$  is averaged over the buoyant layer of thickness h defined following Arneborg et al. (2007) as:

$$h = \frac{2\int_{-D}^{0} (\rho_0 - \rho)z dz}{\int_{-D}^{0} (\rho_0 - \rho)dz}.$$
 (6)

Note  $F_i$  < 1 corresponds to the supercritical regime ( $F_i$  should only be considered within the plume as the ambient ocean is unstratified).

#### 178 3. Results

Here we present the suite of model simulations summarized in Table 1 aimed at studying the 179 emergence and breakdown of the cross-shelf plume regime. We begin by considering a case 180 without wind forcing. After establishing the dynamical regime of the unforced plume, we add a light upwelling-favorable wind forcing to our model. This leads to the striking emergence of the 182 cross-shelf plume regime, which persists under a variety of inflow conditions. Finally, we consider 183 under which forcing conditions the cross-shelf regime breaks down. To further support these findings we perform an ultra-high resolution simulation of the nominal cross-shelf plume case. We find that although the dynamics broadly converge between the lower and higher resolution cases, 186 the latter offers novel insights into the submesoscale mixing phenomena leading to mixing within 187 the plume. We devote the last subsection of the results to examining the higher-resolution case and the submesoscale mixing dynamics captured there. 189

# a. The Unforced, Coastally-Trapped Plume

We start by considering a rotational plume under no wind forcing (case SNW in Table 1). 194 The buoyant inflow conditions at the mouth can be characterized as supercritical and high Bu, 195 implying strong momentum advection, separation of the buoyant layer from the frictional bottom, and initial radial spreading of buoyant water from the mouth. Such buoyancy forcing represents 197 a classical subject in plume research and has been extensively studied (e.g., Chao and Boicourt 198 (1986); Garvine (1987); Oey and Mellor (1993)). Rotational, buoyant plumes under no wind forcing consist of four regions (see Horner-Devine et al. (2015), Figure 2 for a schematic). The 200 source region extends from the river mouth to the liftoff location, where the buoyant plume loses 201 contact with the bottom. The jet-like near-field region follows; here the momentum of the plume 202 dominates over other forces, resulting in strong mixing. In the mid-field region, the plume is increasingly dominated by Earth's rotation, forming an anticyclonic circulation (bulge). Finally, 204 the far-field region of the plume is a geostrophic coastal current that carries the riverine water along 205 the coast in the direction of Kelvin wave propagation.

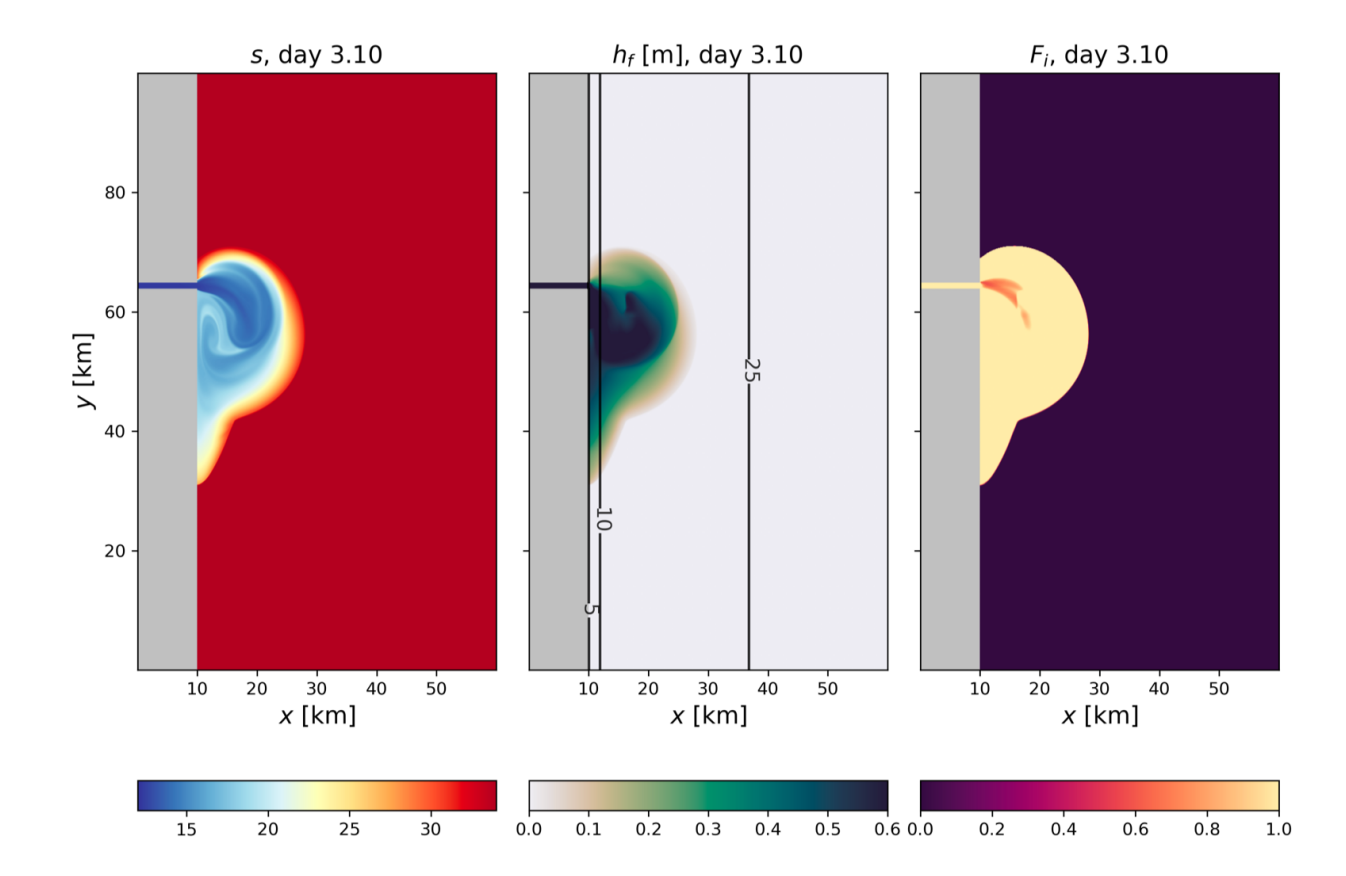


Fig. 1. No wind forcing case (SNW in Table 1), left to right: surface salinity, equivalent freshwater layer thickness ( $h_f$ ), and inverse Froude number ( $F_i$ , with  $F_i$  < 1 being supercritical). Isobaths are shown in the middle panel.

The plume shown in Figure 1 behaves as we expect from a high Bu, supercritical inflow, initially forming a thin layer that spreads radially with the ebbing tidal pulse (seen in the salinity field). The plume's front advances following each tidal cycle in the form of an internal bore. The plume is shaped by Earth's rotation, developing a mid-field anticyclonic bulge and a far-field coastal current after just five tidal cycles. The flow is supercritical only near the mouth but then transitions to the subcritical regime ( $F_i > 1$ ). The plume spreads as a thin, 2 m deep buoyant layer (Figure 2), which is roughly comparable to the Ekman depth

$$h_E = \sqrt{(2A_z/f)}. (7)$$

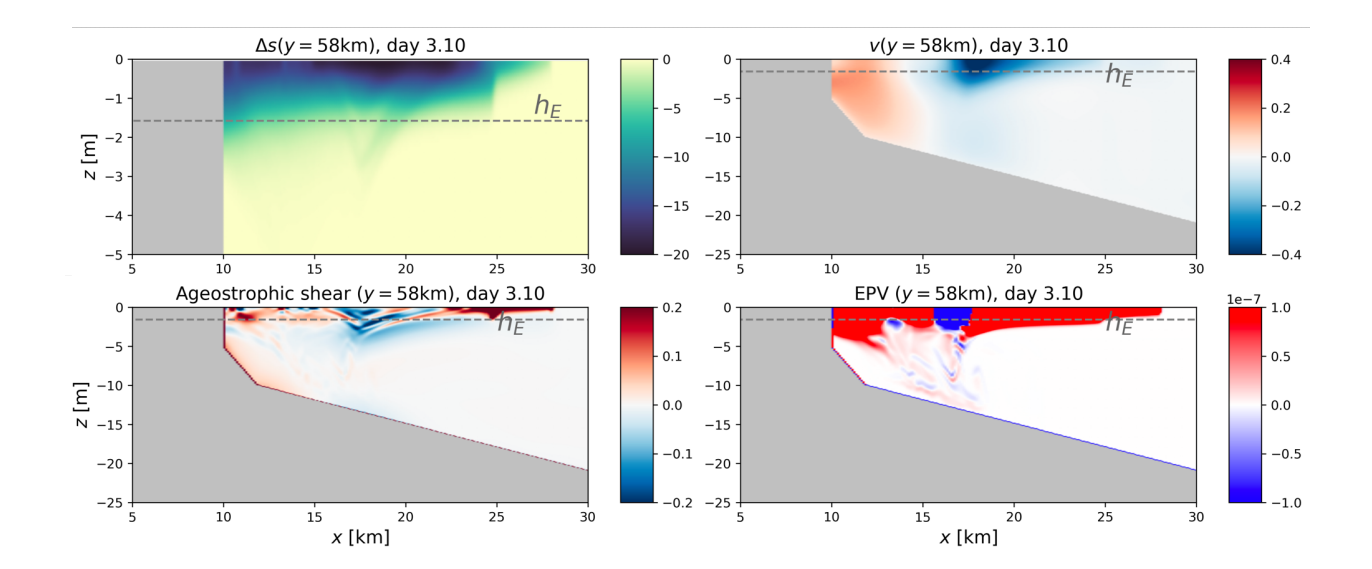


Fig. 2. No wind forcing case (SNW), vertical transects are taken across the plume at y = 58 km and 3.10 days. Upper left panel is the salinity anomaly  $\Delta s$  with Ekman depth  $h_E$  marked, upper right is the alongshore velocity component v, lower left is the ageostrophic shear, and lower right is the Ertel potential vorticity. Note the smaller vertical scale of the upper left plot.

Having a sufficiently small  $h_E$  in our model ensures that the wind forcing imposed in subsequent numerical experiments does not artificially deepen the surface boundary layer to significantly exceed the buoyant layer depth. The alongshore velocity v is characterized by strong vertical shear. However, the shear deviates from the geostrophic shear component; this is expected in rotational plumes, but at a later stage of their development and farther away from the source. Ageostrophic shear is the difference between vertical shear  $(\partial v/\partial z)$  and thermal wind shear  $(\partial v_g/\partial z)$ :

$$\frac{\partial v}{\partial z} - \frac{\partial v_g}{\partial z} = \frac{\partial v}{\partial z} - \frac{-g}{f\rho_0} \frac{\partial \rho}{\partial x}.$$
 (8)

The ageostrophic shear field (Figure 2, lower left) shows the presence of beam-like structures of alternating sign. These beams are reminiscent of inertial-symmetric instability (ISI), which develops in frontal regions with strong geostrophic shear (Grisouard 2018). Pure symmetric instability (SI) extracts energy from the flow through the vertical geostrophic shear production (GSP) term

$$GSP = -\overline{\hat{v}} \hat{w} \frac{\partial \overline{v_g}}{\partial z}, \tag{9}$$

where an overline indicates a spatial average over the SI scale and hats are deviations from the average, whereas pure inertial instability (InI) extracts energy through the lateral shear production (LSP) term (Thomas et al. 2013; Wenegrat and Thomas 2020):

$$LSP = -\overline{\hat{v}}\hat{u}\frac{\partial \overline{v_g}}{\partial x}.$$
 (10)

SI, InI, and ISI hybrids (energized through a combination of GSP and LSP) may be diagnosed by computing the Ertel potential vorticity (EPV):

$$EPV = (f\hat{\mathbf{k}} + \nabla \wedge \mathbf{u}) \cdot \nabla b, \tag{11}$$

where buoyancy is defined as  $b = -g\rho/\rho_0$ .

When the EPV is opposite in sign to the Coriolis parameter and the flow is gravitationally stable, 236 the condition for instability is met (Hoskins 1974). In Figure 2 we see that the beam-like structures 237 originate in the area of negative EPV, indicating ISI. Based on Equations 9-11, we identify SI, InI, and hybrid ISI depending on the orientation of the front relative to the background geostrophic current (discussed in greater detail in Section 4). Interestingly, the salinity anomaly (Figure 2, upper 240 left) shows beams of freshwater propagating downwards and being mixed. ISI provides a mixing 241 mechanism that erodes and deepens the plume front. Although SI was previously identified in realistic regional simulations (Ayouche et al. 2020, 2021) and in idealized process studies (Lv et al. 243 2020), it arose in the presence of wind forcing and with several times coarser spatial resolutions. 244 Ayouche et al. (2020, 2021) found that the Hoskins instability criterion for SI is satisfied in frontal regions within the Gironde plume in the Bay of Biscay. However, their model had horizontal 246 resolutions of 200-400 meters and vertical resolutions on the order of 10s of meters. Similarly, 247 horizontal resolutions in Lv et al. (2020) were 1-2 km. As a result, the vertical shears and velocity 248 beams driven by SI (and ISI hybrids) evolving on horizontal scales of hundreds of meters and vertical scales of 1-10s of meters were under-resolved (Bachman et al. 2017). In our domain, we 250 achieve resolutions of 0.1 meters vertically and 100 m horizontally (15 meters in our ultra-high 251 resolution case, Section 4). We are thus able to capture the vertical ISI beams as well as some of the secondary mixing and frontal erosion. Thus, we have considered a case with no wind forcing 253 to simulate the well-studied coastally-trapped regime ubiquitous among natural river plumes. We 254

established that our model accurately represents the dynamics arising in a rotational river plume. Additionally, owing to the high resolution of our model we identified a new mixing pathway arising in this regime. The buoyant inflow advects negative EPV into the domain, which gives rise to inertial-symmetric instability. ISI creates diagonal ageostrophic velocity beams that lead to mixing of plume tracers and deepening of the plume front. We will next consider what happens when a light northward (upwelling-favorable wind) is incorporated into our model.

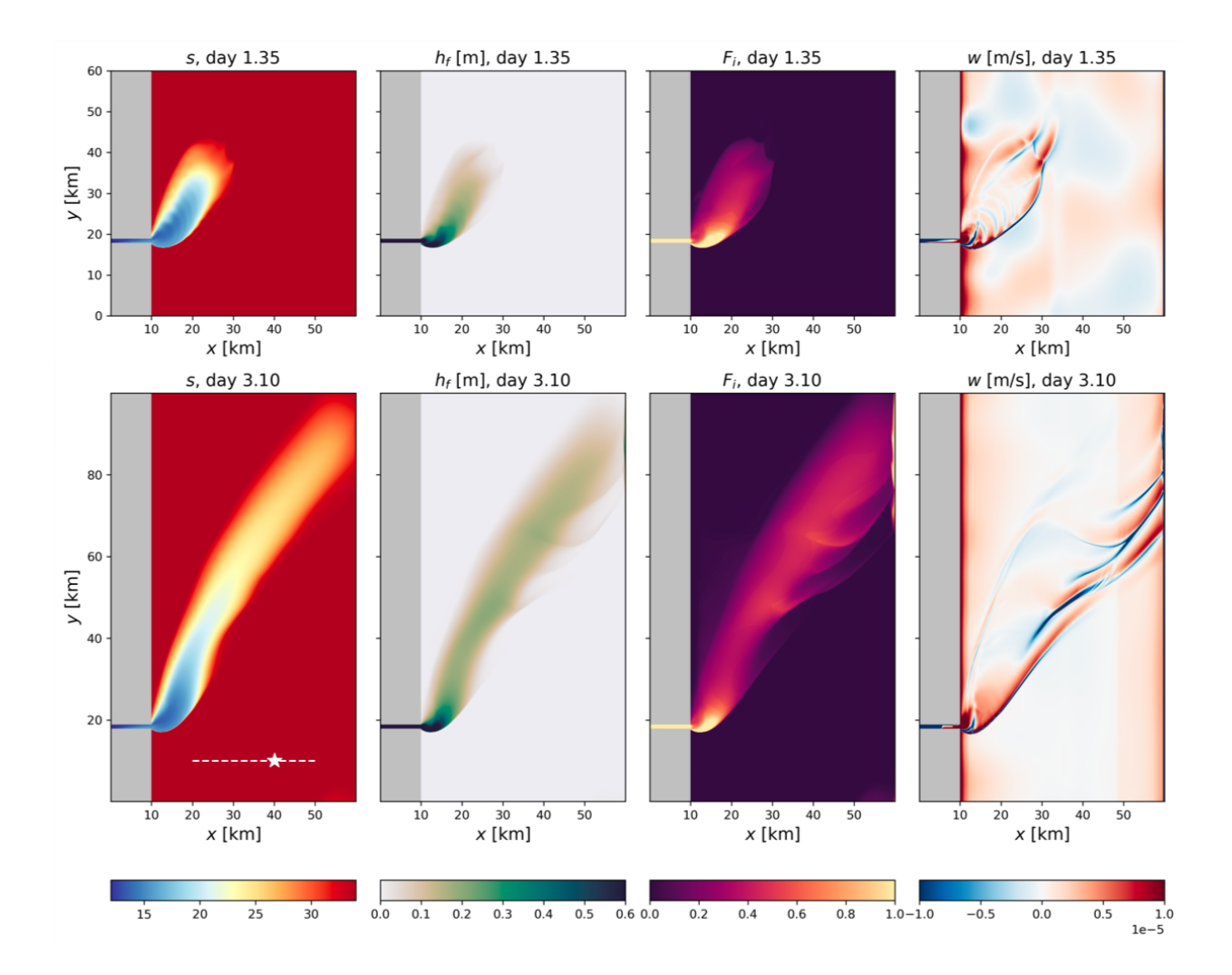


Fig. 3. Standard case without tides (SNT), fields are shown at days 1.35 (upper row) and 3.10 (lower row). Left to right: surface salinity, equivalent freshwater layer thickness ( $h_f$ ), inverse Froude number ( $F_i < 1$  is supercritical), and vertical velocity (w). The star and dashed line in the lower left panel indicate where the Ekman velocity and geostrophic velocity are computed in Figure 4.

# 5 b. The Cross-Shelf Regime

#### 1) Overview

266

After establishing the coastally-trapped plume regime in the prior section, we add a temporally 267 constant wind forcing of 0.03 Pa to our model (case SNT, Table 1). The wind is directed northward, 268 thus upwelling-favorable, and discharge is constant in time following the initial ramp-up (no tidal modulations). The evolution of the plume is shown in Figure 3. We see a stark contrast with 270 the alongshore regime discussed prior. Rather than forming a bulge and deflecting back towards 271 the coast in a geostrophic current, the plume detaches from the coast and spreads upstream and offshore, curving slightly to the right with distance from the mouth. It retains a tight transverse 273 structure (seen in the salinity field), that is, it does not broaden substantially with distance from its 274 source. Salinity increases towards the flanks of the plume due to mixing, but we do not see the 275 radial spreading characteristic of the prior SNW case.

We observe radiation of solitary internal waves (Apel et al. 2007) at the upstream (northward) 277 flank of the plume and propagating in the downstream (southward) direction. These solitons are 278 seen in the freshwater content field as curving lines of higher  $h_f$  values. Due to superposition of the wind-induced drift, we also see that the plume remains supercritical as it moves offshore 280 (Fi< 1, Figure 3). By transporting mass and momentum into the interior and downstream part 281 of the plume, the solitons suppress mixing at the northward edge and prevent the plume from spreading laterally. The plume remains coherent and supercritical over the cross-shore extension 283 of the numerical domain through this mechanism, described in greater detail below. Figure 3 284 shows two time snapshots: day 1.35, when the first soliton is clearly formed, and day 3.1 (the end 285 of integration). Solitons can also be identified in the vertical velocity component w as localized 286 areas of high negative values (shown in blue in Figure 3), residing within the plume. 287

# 288 2) BACKGROUND FLOW DYNAMICS

We now address the dynamics of the cross-shelf plume in detail, first considering the background flow onto which the plume is superimposed. We choose locations outside of the plume, shown as a transect and star in Figure 3. The background flow dynamics include: (i) surface windinduced eastward Ekman flow; (ii) an along-channel geostrophic current driven by the crosschannel pressure gradient (which results from the Ekman transport divergence/convergence at the

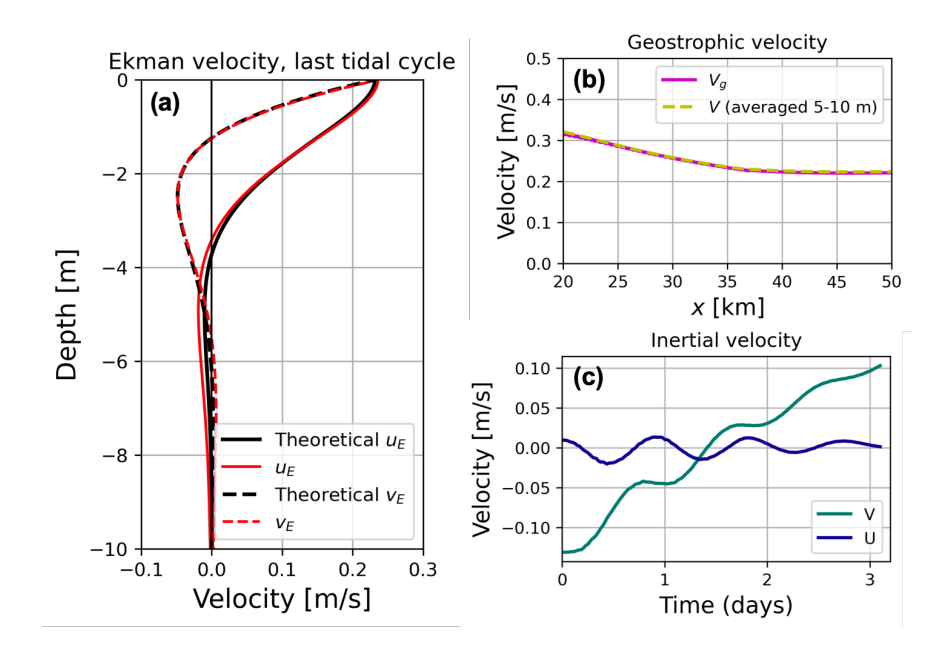


Fig. 4. Standard case without tides (SNT): (a) theoretical and observed Ekman velocity components ( $u_E$ ,  $v_E$ ) as a function of depth and averaged over the last tidal cycle at the starred location in Figure 3, (b) theoretical geostrophic velocity  $v_g$  and observed v (alongshore velocity averaged over 5-10 meters) also averaged over the last tidal cycle, and (c) inertial velocity components at the same location as (a) at 12.5 m depth, shown as a function of time.

290

293

western/eastern wall, respectively), and (iii) decaying near-inertial oscillations. These features
are shown in Figure 4. In panel (a), we computed the observed Ekman velocity components by
averaging the horizontal velocities over the last tidal cycle and subtracting the mid-depth velocity.
The vertical structure of these velocities is in near-perfect agreement with the well-known Ekman
solution in the surface boundary layer outside of the plume:

$$(u_E, v_E) = \frac{\tau e^{z/h_E}}{\rho_0 \sqrt{A_z f}} (\cos(\pi/4 + z/h_E), \sin(\pi/4 + z/h_E)).$$
(12)

The location is shown as a star in Figure 3 and is not affected by the presence of buoyant water

(and hence the associated baroclinic velocity shear). The geostrophic along-channel current also

generates compensating westward Ekman transport near the bottom (not shown). The along
channel velocity averaged over 5-10 meters depth, outside of the surface and bottom boundary

layers and away from coastal walls, is shown in panel (b) to be in geostrophic balance with the

barotropic cross-shore pressure gradient set by the sloping sea surface. Lastly, in panel (c) we obtained the mid-depth velocity as a function of time and subtracted its temporal mean, for the same location as panel (a). Both u and v velocity components exhibit weak velocity oscillations with periods close to the inertial period of 21.82 h. These features validate the physical behavior of our model, as it exhibits all the theoretical expectations for flow dynamics outside the plume.

# 3) Momentum Balance within the Plume and Internal Wave Generation

The momentum balance within the plume region is assessed at 1.35 days, the time when soliton radiation begins (Figure 5). To eliminate the surface wind stress term, we consider the first grid cell below the surface (0.1 m depth). The leading-order terms both outside and inside the plume are the cross-shelf pressure gradient, Coriolis force, and vertical divergence of shear stresses. Although the viscous term combines both horizontal and vertical components, the former is negligible except for the upwind frontal interface (not shown). The inertial term reveals internal wave motions: radiating from the mouth and radiating southward from the upstream (northward) flank of the plume. In addition, there are streaks of momentum advection along the upwind part of the plume, negative in *x*-momentum balance and positive in *y*-momentum balance, which overlap with the maximal downward vertical velocity associated with the soliton generation (second column, Figure 5).

The momentum balance shown in Figure 5 is too complex to explain the process of internal wave generation in the offshore part of the plume, although it suggests that the momentum advection terms may be responsible. We further investigate this process through several steps. In Figure 6a, we show the near surface flow field (u', v') where the wind-driven ambient flow  $(u_a, v_a)$  is subtracted:

$$(u', v') = (u - u_a, v - v_a).$$
 (13)

Here  $(u_a(y), v_a(y))$  are taken outside of the plume and the flow field is again considered at 0.1 m depth (first interior grid point). Primed variables represent plume dynamics and along with the freshwater layer topography show the disturbance at  $\sim (20 < x < 30 \text{ km}, 35 < y < 45 \text{ km})$  which subsequently propagates as an internal soliton. In Figure 6b, the same field is shown for a model run where the momentum advection is turned off. Without the nonlinear terms, no perturbations occur at the advancing edge of the plume. Horizontal current vectors at the advancing edge are outward of the plume (near perpendicular to local  $h_f$  contours), consistent with the dynamics of the

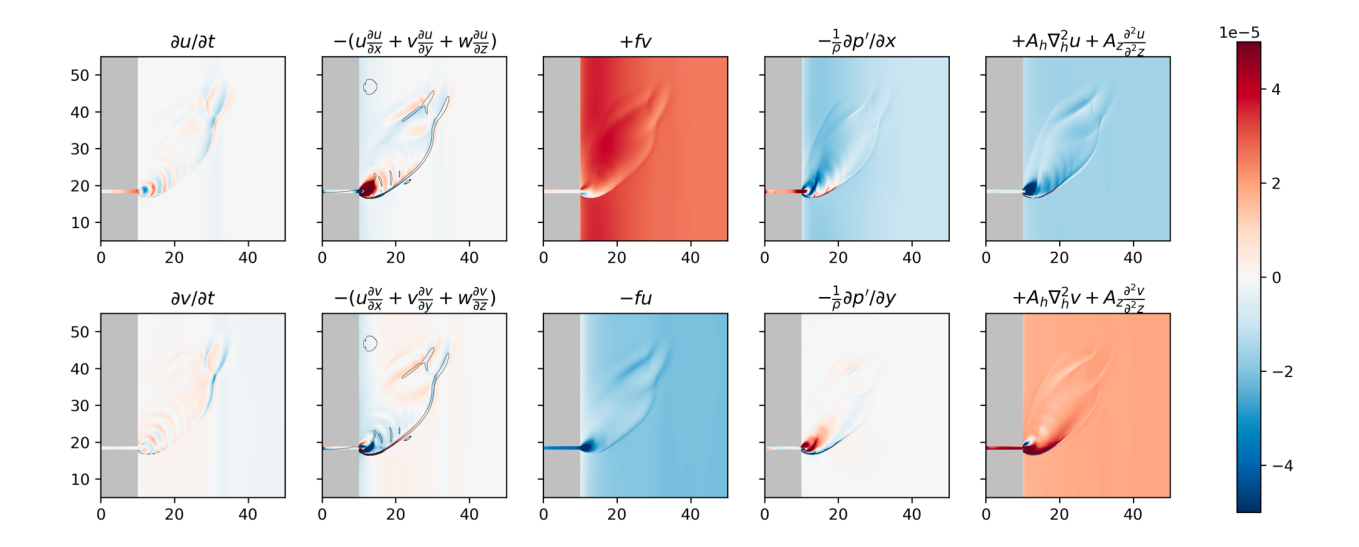


Fig. 5. Standard case without tides (SNT): top row shows the zonal momentum budget and bottom row shows the meridional momentum budget at 1.35 days at 0.1 m depth. Terms are denoted in each subplot's title, left to right: time tendency, advection, Coriolis, pressure gradient, and viscous terms. The second column includes an isoline of vertical velocity w (at the value  $-2 \cdot 10^{-6}$  m s<sup>-1</sup>).

gravity current, while behind the leading edge (closer to the mouth) velocity adjusts geostrophically and becomes more aligned with local  $h_f$  contours. It is clear at this point that the internal wave radiation in the offshore segment of the plume is due to the momentum advection associated with the ambient wind-driven flow field, since neither the linear solution of this model experiment, nor the nonlinear unforced plume (Figure 1) give rise to internal waves offshore.

Next, we construct a simplified momentum balance with nonlinear terms which is applied to the linear solution's flow field along the transect x = 20.5 km, 35 < y < 45 km shown in Figure 6b. This transect approximately represents the locus of the maximum freshwater content, the most downwind-protruding part of the plume, and is also the area where the internal soliton originates in the nonlinear solution (Figure 6a). We assume that the wind-induced ambient flow is independent of the alongshore coordinate y. Furthermore, at the offshore location of this transect, the Ekman dynamics are fully developed, and  $u_a$  is assumed to be spatially uniform. Subtracting equations for  $u_a$  and  $v_a$  from the total momentum balance equations yields:

$$\frac{\partial u'}{\partial t} + (u' + u_a) \frac{\partial u'}{\partial x} + (v' + v_a) \frac{\partial u'}{\partial y} - fv' = -\frac{1}{\rho} \frac{\partial p'}{\partial x} + A_z \frac{\partial^2 u'}{\partial z^2},\tag{14}$$

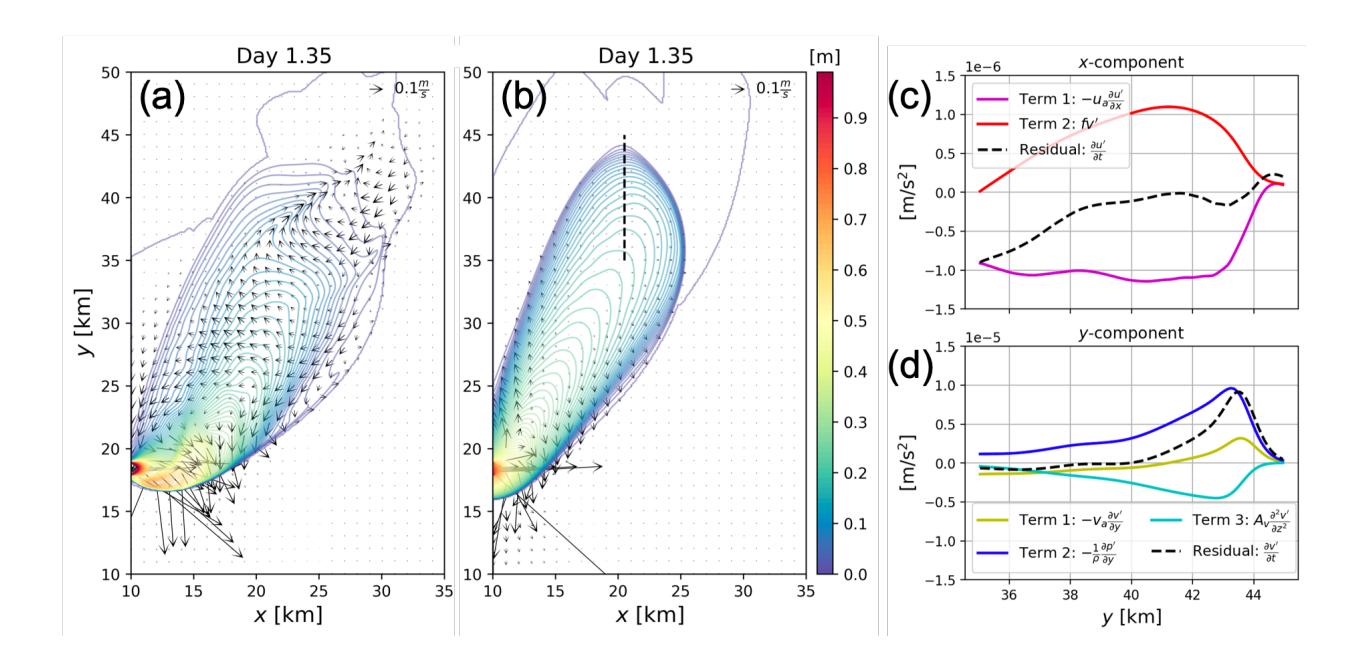


Fig. 6. (a) Standard case without tides (SNT): Freshwater layer thickness  $h_f$  (shown as colored contours) and the near-surface velocity field (shown as vectors) associated with the plume at 1.35 days when solitons develop on both sides of the divergent segment of the plume. The velocity associated with the plume is computed by subtracting the surface velocity defined along a zonal transect at y = 60 km (outside the plume) from each zonal transect in the domain. (b) Same as (a), but for a simulation where the momentum advection in the model has been turned off. Dashed black line shows the transect for which the momentum balance in panels (c)-(d) is computed. (c) Momentum balance based on Equation 16. (d) Momentum balance based on Equation 17.

$$\frac{\partial v'}{\partial t} + (u' + u_a) \frac{\partial v'}{\partial x} + u' \frac{\partial v_a}{\partial x} + (v' + v_a) \frac{\partial v'}{\partial y} + fu' = -\frac{1}{\rho} \frac{\partial p'}{\partial y} + A_z \frac{\partial^2 v'}{\partial z^2}.$$
 (15)

Here p is the pressure; the horizontal viscosity is ignored because it is important only at the upwind front, and the vertical momentum advection is ignored because the ambient flow has small vertical velocities at this offshore location. Next, we assume that since velocities at the leading edge of the plume are smaller than the wind induced advection, the nonlinear terms associated with the plume dynamics alone (products of primed variables) can also be discarded. Lastly, along the locus of the  $h_f$  maximum several other simplifications can be made:  $\frac{\partial p'}{\partial x}$ , u',  $\frac{\partial u'}{\partial y}$ ,  $\frac{\partial v'}{\partial x} = 0$ . These assumptions for velocity and its derivatives are based on the near-normal velocity orientation with respect to  $h_f$  contours at the leading edge of the plume. With these assumptions, the momentum balance equations are reduced to:

$$\frac{\partial u'}{\partial t} = -u_a \frac{\partial u'}{\partial x} + f v', \tag{16}$$

$$\frac{\partial v'}{\partial t} = -v_a \frac{\partial v'}{\partial y} - \frac{1}{\rho} \frac{\partial p'}{\partial y} + A_z \frac{\partial^2 v'}{\partial z^2}.$$
 (17)

We treat the linear solution (Figure 6b) as the mean, unperturbed state of the plume, and we 370 estimate nonlinear terms in Equations 16 and 17 from this state. If these nonlinear terms are 371 permitted, they should lead to the perturbation similar to that shown in Figure 6a. Without the 372 advective terms, the momentum balance will lead to geostrophic adjustment (which has already 373 formed closer to the mouth in Figure 6b): the outward v momentum will be turned offshore through 374 the Coriolis effect  $(\frac{\partial u'}{\partial t} > 0$  in the x-momentum balance), and the northward pressure gradient force 375 in the y-momentum balance will be balanced by the resulting Coriolis force fu'. The balance will 376 not be purely geostrophic due to the contribution of the vertical eddy viscosity. 377

This situation changes drastically when the nonlinear terms are present (Figure 6c, d). In the x-momentum balance, the offshore advection (through the Ekman transport) of u' counteracts 379 the Coriolis force, and hence prevents geostrophic adjustment (that is, clockwise turning of the 380 velocity vector is suppressed). In fact, for y < 40 km, the acceleration is negative, giving rise to the along-front flow in the onshore direction, opposite to geostrophic flow. In the y-momentum balance, the advective term changes sign and becomes positive (adding to the northward pressure 383 gradient force) at y = 41 km, and its magnitude exceeds the vertical viscosity term at the edge of the plume. As a result, the v' acceleration matches (or even exceeds) the pressure gradient force for y > 43 km. These two conspicuous features are seen in the offshore and downwind segment 386 of the plume (x > 20 km, 35 < y < 45 km) in the nonlinear solution (Figure 6a): the onshore flow 387 along  $h_f$  contours (against the geostrophic direction) and the northward/offshore jet crossing the front and exiting the plume. This flow pattern results in a crest-like structure of the buoyant layer 389 thickness, which subsequently radiates southward as an internal soliton. 390

Finally, it should be noted that the internal wave generation is expected to be highly sensitive to the vertical eddy viscosity, since this is the only term opposing the combined effect of the pressure gradient and momentum advection in Equation 17 at the edge of the plume. Its role will be further discussed in the next section.

392

393

- Thus, we summarize the maintenance of the cross-shelf plume regime as follows:
- 1. The advection of plume momentum by the ambient wind driven flow prevents geostrophic adjustment after the passage of the plume's leading edge. Instead, the offshore part of the plume continuously radiates internal solitons (see animations in supplementary material).
- 2. Solitons radiate into the plume (upwind), transporting mass and momentum and preventing downwind diffusion of the plume. Solitons are suppressed beyond the plume's boundaries as they cannot propagate into unstratified water. Thus, the plume remains supercritical and retains its coherence as it propagates further offshore.

# 403 4) PARAMETER SPACE OF THE CROSS-SHELF REGIME

Here we perform a sensitivity study to delineate the parameter space under which the cross-408 shelf regime persists. We add a tidally modulated estuarine inflow to our model configuration 409 (Figures 7 and 8). We investigate whether variable discharge, which enhances nonlinear advection 410 of momentum in the near field, has an effect on the dynamics previously identified for the constant discharge case. We then modify several model parameters to asses the conditions under which 412 the cross-shelf regime persists vs. breaks down. Case S in panel (a) is the standard case and is 413 analogous to the previously considered SNT (see Table 1). The plume structure is more complex that in Figure 3 and comprises tidal sub-plumes partially separated by gaps in salinity and  $h_f$ . 415 These gaps gradually merge in the older part of the plume. The number of solitons seen in the  $h_f$ 416 panel (Figure 8a) has increased compared to the case with steady-state inflow (Figure 3); in this case each tidal cycle produces a soliton. In the two next cases (Figures 7-8, b-c) the mouth width 418 increases such that Bu drops to 1.12 for W = 5 km and to 0.51 for W = 10 km. When Bu < 1 in 419 an unforced (no wind) plume, there is a tendency for geostrophic adjustment of the inflow, with the nonlinear momentum advection becoming negligible. In panels (b-c) we see that tidal sub-421 plumes become progressively less distinct with increasing W. However, the cross-shelf regime still 422 persists even when Bu < 1, albeit with slightly reduced overall offshore extension of the buoyant 423 layer. The mechanism described above for the maintenance of the cross-shelf regime by soliton radiation continues to operate and the resulting plume retains its narrow transverse structure. The 425 cross-shelf plume regime breaks down in the case with stronger wind stress and enhanced vertical 426 eddy viscosity/diffusivity coefficients (Figures 7-8d, case V2W10 in Table 1). In this case the

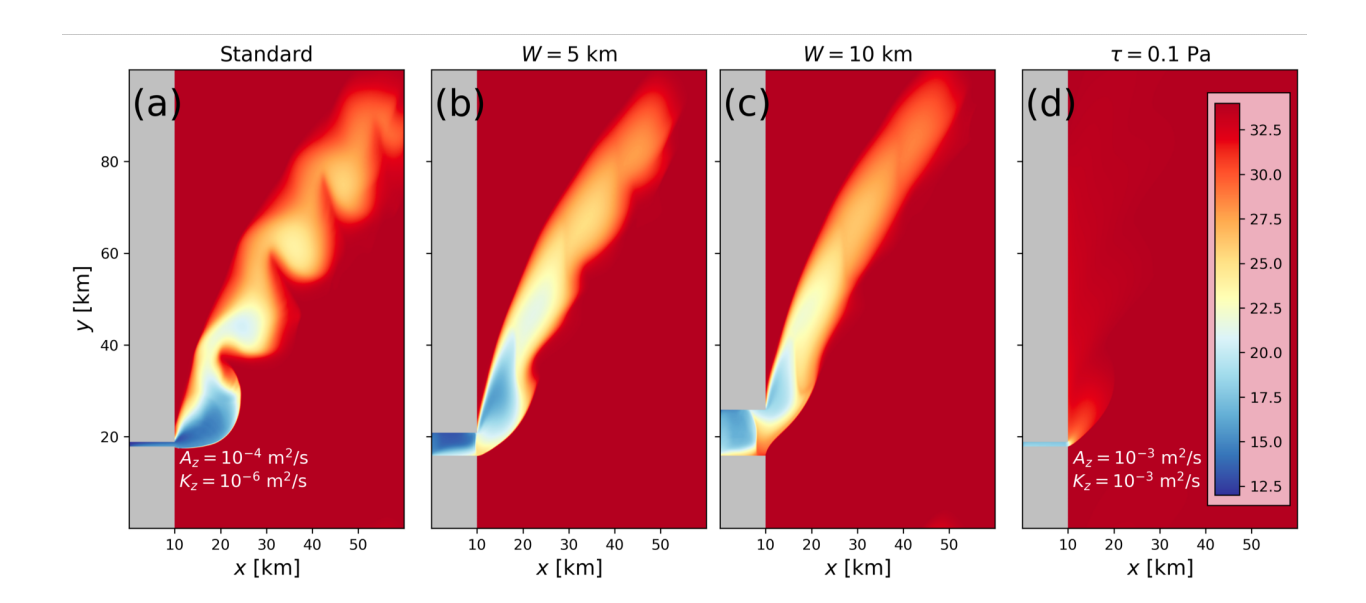


Fig. 7. Surface salinity at 3.1 days for four cases: (a) standard (S), (b) 5 km wide mouth (SM5), (c) 10 km wide mouth (SM10), (d) highest wind forcing and higher viscosity and diffusivity values (V2W10). In cases S, SM5, and SM10 the vertical viscosity is  $A_z = 10^{-4}$  m<sup>2</sup> s<sup>-1</sup> and vertical diffusivity is  $K_z = 10^{-6}$  m<sup>2</sup> s<sup>-1</sup>, while in case V2W10,  $A_z = 10^{-3}$  m<sup>2</sup> s<sup>-1</sup> and  $K_z = 10^{-3}$  m<sup>2</sup> s<sup>-1</sup>.

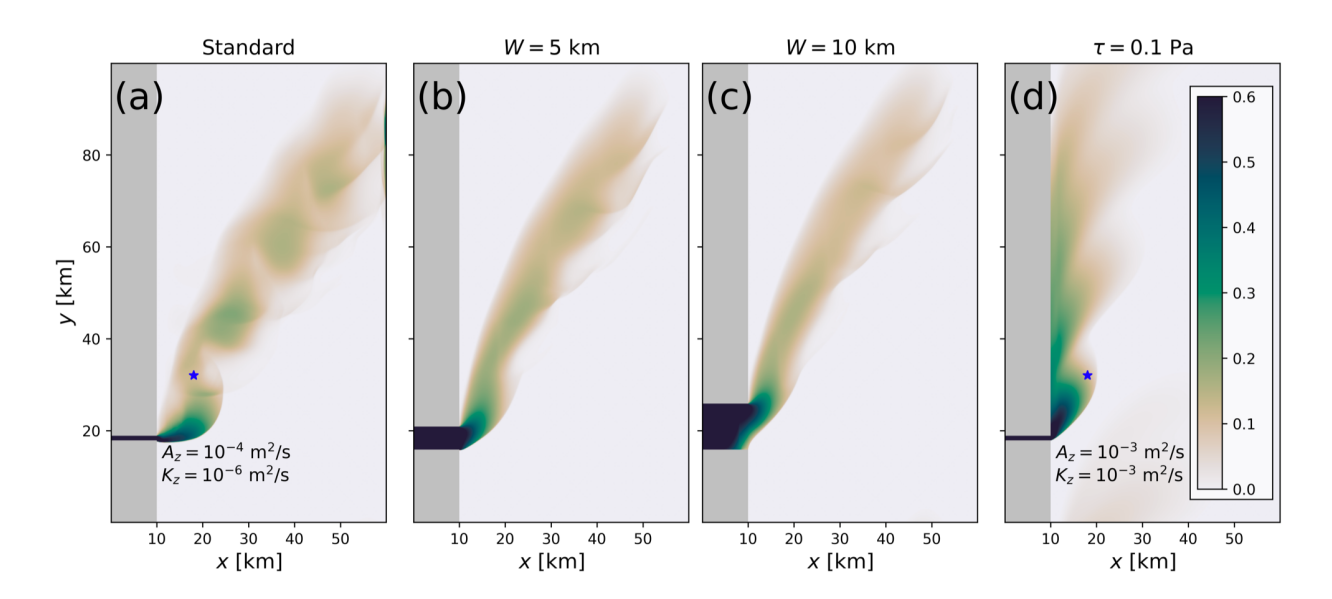


Fig. 8. Equivalent freshwater layer thickness  $h_f$  at 3.1 days for the same cases as Figure 7.

plume spreads predominantly alongshore in the upstream direction, with some offshore Ekman transport. The salinity signal is very weak (the same color scheme is used for all panels in Figure 7), and the largest concentration of freshwater is along the coast.

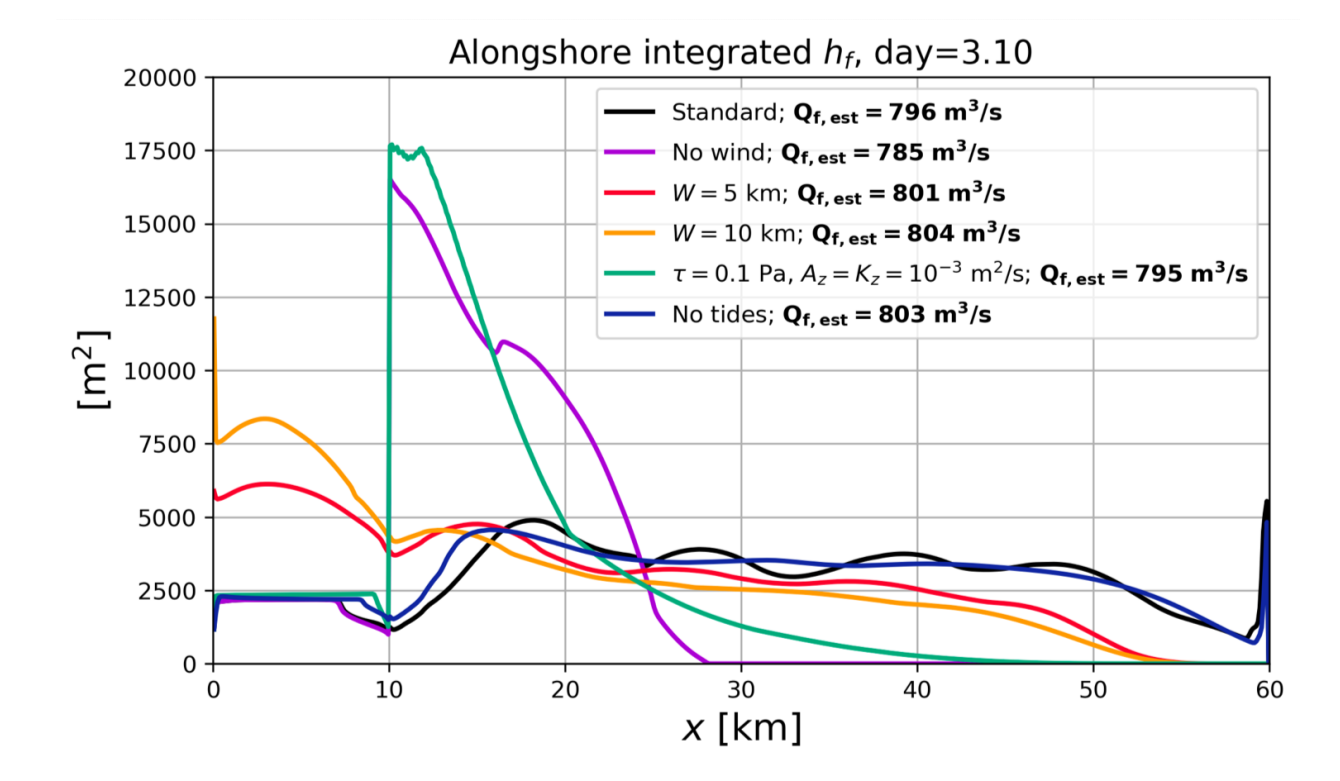


Fig. 9. Alongshore integrated equivalent freshwater layer thickness  $h_f$  as a function of offshore distance x for a suite of cases, top to bottom: S, SNW, SM5, SM10, V2W10, and SNT. Shown in the legend is the apparent freshwater discharge for each case (this quantity should be 800 m<sup>3</sup> s<sup>-1</sup>, and is used as a measure of model performance).

Cross-shore transport of freshwater associated with the cross-shelf plume is delineated in Figure 9, where  $h_f$  (Equation 4) is integrated along the channel. This integral, when divided by the duration of the inflow (five tidal cycles) also yields an offline estimated freshwater discharge ( $Q_{f,est}$ ), which can be compared against the nominal freshwater discharge of 800 m<sup>3</sup> s<sup>-1</sup> to gauge model error. In all but one case shown in Figure 8 the discrepancy is less than 1%, which is a very commendable performance of the model. The only case with larger than 1% discrepancy is the SNW case without wind stress (785 vs. nominal 800 m<sup>3</sup> s<sup>-1</sup>), where the horizontal advection of salinity is the lowest among all cases considered.

The freshwater distribution across the channel with and without tidally modulated inflow is nearly identical (Figure 9), with some freshwater accumulating at the eastern wall of the channel. The tendency for offshore freshwater accumulation increases with wind stress increase, for a given eddy viscosity value (cases SW5 and SW10, see below). The cross-shore freshwater delivery is reduced

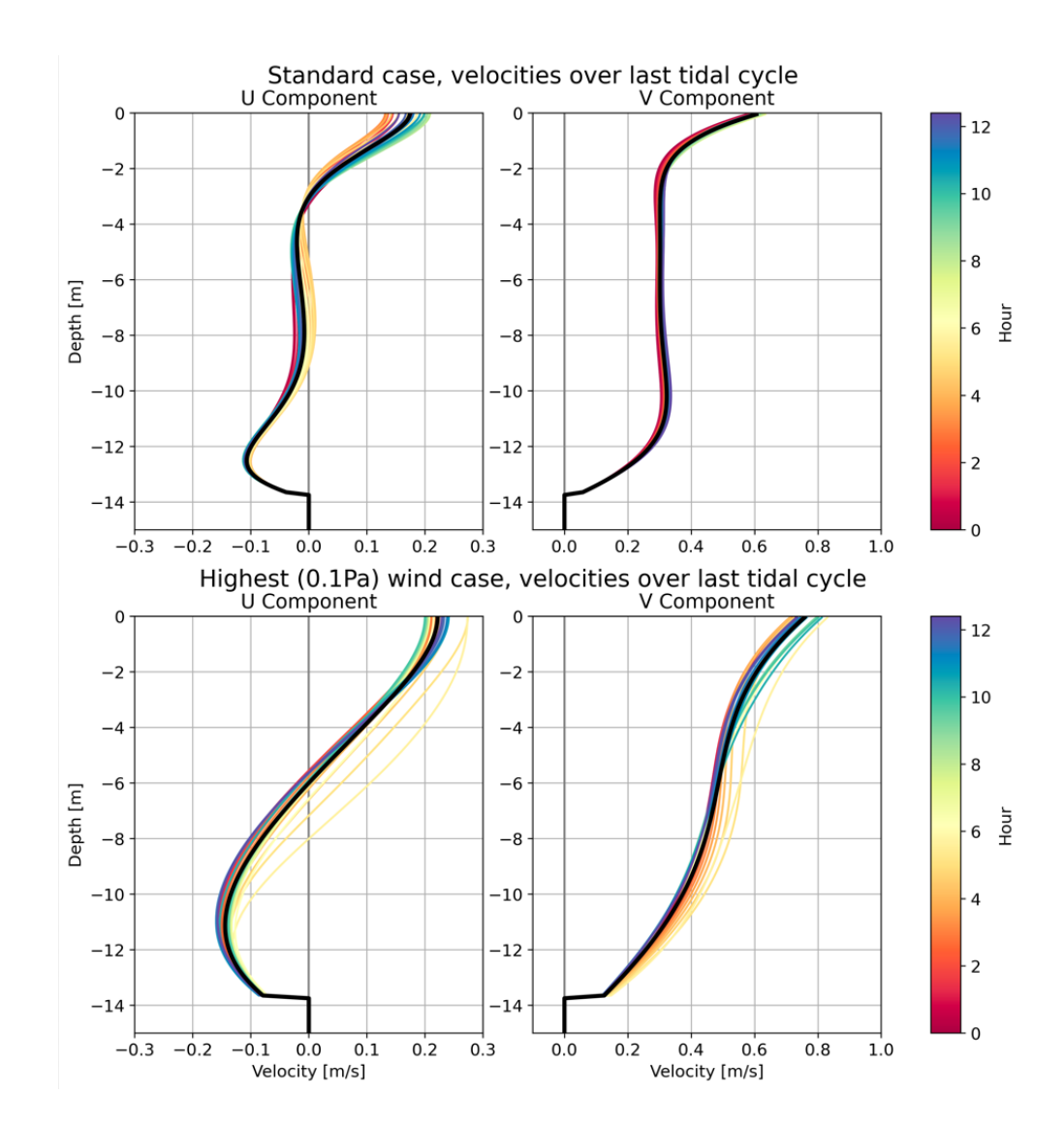


Fig. 10. Vertical profiles of horizontal velocity components (u, v) within the plume at the location marked as a blue star in Figure 8. Velocity profiles are shown as snapshots every half hour for the last tidal cycle (color corresponds to time of the snapshot); the time-averaged profile is shown in black. The top row is for case S (standard) and the lower row for case V2W10 (highest wind forcing and higher viscosity and diffusivity values).

437

438

in the cases with wider mouths, but this reduction is primarily due to accumulation of freshwater in the estuary. To better quantify the cross-shore transport of buoyant water, the following coefficient for the offshore freshwater delivery is used:

$$R_f = \frac{\int_{x=35}^{x=60} h_f dx}{\int_{x=10}^{x=60} h_f dx},$$
(18)

where  $R_f$  is the ratio of the freshwater volume advected past the channel midpoint at x = 35 km to 454 the total amount of freshwater advected past x = 10 km, which is the mouth location. See Table 1 for 455 values of  $R_f$  for each experiment. We find  $R_f$  weakly depends on the estuarine Bu (i.e., decreases 456 from 0.29 to 0.25 as Bu decreases from 1.12 to 0.51, cases SM5 and SM10) and the presence of tidal modulation (i.e., increases from 0.44 to 0.45 between cases SNT and S). On the other hand,  $R_f$ 458 drastically increases with increasing wind stress when  $A_z$  and  $K_z$  are kept constant, as in cases S, 459 SW5, and SW10 at 2.3 days (increasing from 0.19 to 0.45 to 0.60 between the cases). The latter is a somewhat unrealistic proposition as both  $A_z$  and  $K_z$  are likely to increase with wind stress; these 461 experiments are simply meant to emphasize the role of the advection when the vertical viscosity and 462 diffusivity are both low. Once  $A_z$  and  $K_z$  are increased,  $R_f$  is dramatically reduced. In particular, 463 cases S and V2W10 have almost the same depth-averaged Ekman velocities: 0.23 and 0.24 m 464 s<sup>-1</sup>, respectively, which are estimated as  $U_E/h_E$ , where  $U_E = \tau/(\rho_0 f)$  is the Ekman transport. 465 However, in the latter case  $R_f$  is only 0.02 by the end of integration (very little freshwater crosses 466 the channel midpoint), while in the S case  $R_f$  is 0.45. As discussed, case V2W10 demonstrates the breakdown of the cross-shelf plume regime. 468

The vertical structure of horizontal currents near the coast in water depths of less than 14 m 472 is examined for two cases, S and V2W10, in Figure 10. In the standard case S the surface and bottom boundary layers are well separated by mid-depth flow with no vertical shear, while in the 474 case with higher  $A_z$ , the boundary layers overlap and the flow is continuously sheared from the 475 surface to the bottom. This regime is often referred to as the inner shelf dynamics (Lentz 2001), and if  $A_z$  further increases, the veering of the horizontal velocity vector with depth can be reduced 477 and the cross-shelf flow pattern (offshore near-surface and onshore near-bottom) can be severely 478 weakened. In addition, we see an increased alongshore v-component from the S to the V2W10 case 479 due to the wind stress increase, while the cross-shelf velocity remains approximately the same due to deepening of the Ekman layer. Hence, the advection of buoyant water shifts to a predominantly 481 alongshore pathway and the cross-shelf regime is suppressed. 482

The previously considered cases S, SM5 and SM10 all have the same wind-driven circulation (and hence, ambient advection), and the plumes are driven by the same freshwater discharge, making the conditions for internal wave radiation roughly comparable. In case V2W10 the internal wave activity is completely shut down due to the increased viscosity  $A_z$  (Figures 7-8). We now

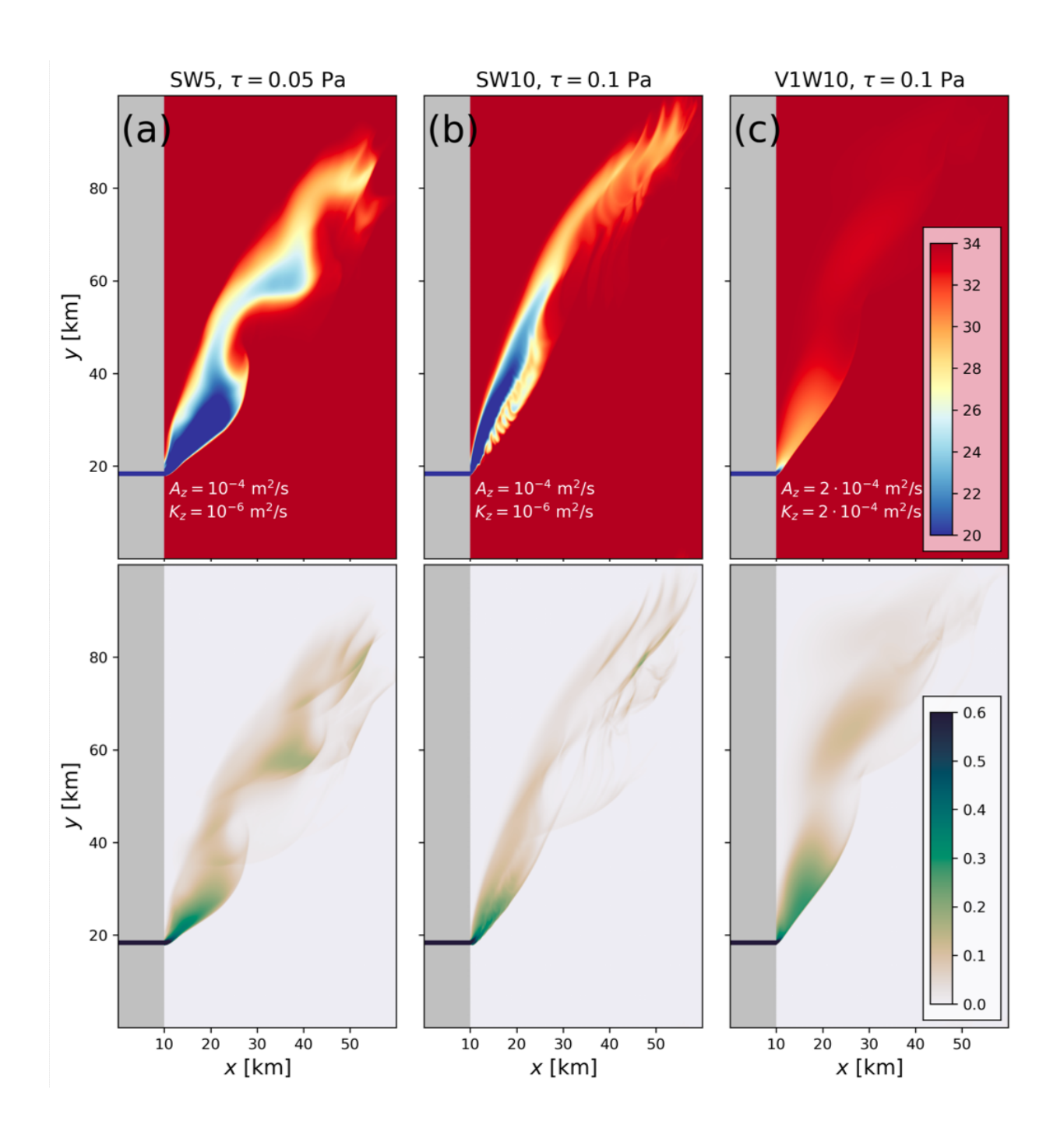


Fig. 11. Surface salinity (top) and equivalent freshwater layer thickness  $h_f$  (bottom). The cases are (left to right): SW5 (with 0.05 Pa wind stress), SW10 (with 0.1 Pa wind stress), and V1W10 (with 0.1 Pa wind stress and higher viscosity and diffusivity values, indicated in the figure).

consider cases where both ambient advection and vertical eddy viscosity change (Figure 11) which should significantly affect the internal wave dynamics as discussed in subsection 3. In model runs

SW5 and SW10, the wind stress increases to 0.05 and 0.1 Pa (compared to 0.03 Pa in case S), 489 leading to faster advection both along- and off-shore. This translates into enhanced generation 490 of internal solitons now seen not only in the  $h_f$  distribution, but in the surface salinity field as 491 well. In particular for case SW10, most of the freshwater is contained in internal solitons, and the offshore plume dynamics (x > 30 km) are now highly nonstationary and nonlinear, without a well 493 defined "bulge". On the other hand, when both vertical viscosity and diffusivity are moderately 494 increased (case V1W10), internal wave activity is significantly reduced (but still present), while the downwind (northern) edge of the plume becomes more diffuse offshore (seen in the  $h_f$  field 496 for x > 25 km). These results indicate that the cross-shelf freshwater transport is most sensitive to 497 the magnitude of the zonal wind stress and vertical mixing coefficients.

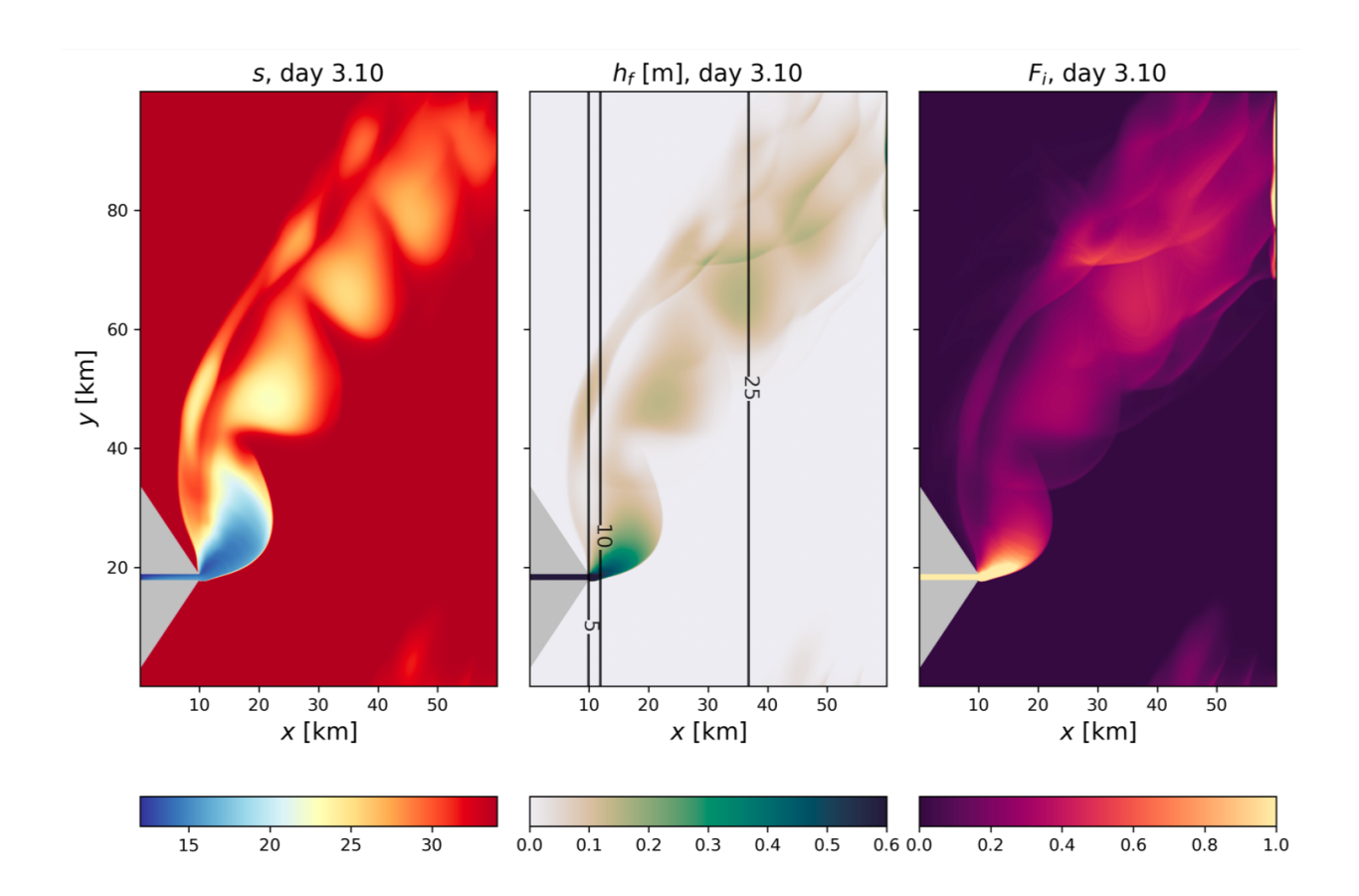


Fig. 12. Case SC, with a coastal promontory corresponding to the idealized geometry of Winyah Bay. Left to right: surface salinity, equivalent freshwater layer thickness  $(h_f)$ , and inverse Froude number  $(F_i < 1)$  is supercritical) at 3.10 days.

499

# 02 5) The Case of a Coastal Promontory

The modeling study presented here has been motivated by observations of the Winyah Bay Plume. 508 The channel of Winyah Bay runs off into the ocean through a coastal promontory formed by barrier islands on both sides of the channel (not a straight coastline as in the idealized cases discussed 510 thus far). In the model run SC, a similar coastal promontory is introduced such that the coastline 511 outside this feature lies at x = 0 km (Figure 12). Otherwise, the model configuration remains the same as in the standard case S. Numerous prior studies have demonstrated that a cape-like coastal 513 feature can lead to a separation of the coastally-trapped buoyant current from the coastline (e.g., 514 Igeta et al. (2017); Whitney (2023); Zhou and Wu (2023)). The resulting plume structure is more complex than in previous cases but there is no additional offshore deflection of the plume compared 516 to case S and the overall offshore delivery of buoyant water in cases S and SC is similar (in fact  $R_f$ 517 is slightly higher in S, see Table 1). The plume now has a longitudinal gap (or discontinuity) in the 518  $h_f$  distribution with two asymmetric parts: the main body and the thin upstream part (the latter is formed when the discharge decreases through the tidal cycle). Both parts of the plume radiate 520 internal solitons in the upwind direction, so that the overall pattern is rather complex in the older 521 parts of the plume farther offshore. We conclude that the existence of a coastal promontory is not crucial for establishing the cross-shelf plume regime of the Winyah Bay outflow. 523

### 4. An Ultra-High Resolution Case

We now present results of an ultra-high resolution simulation, SHR, identical to case S but with a horizontal resolution an order of magnitude finer (Table 1). The vertical resolution is kept the same (0.1 m), but the horizontal resolution is now 15 m (compared to 100 m in case S) in the *x* and *y* directions. The simulation has a time step of 1 second and is computationally expensive; we therefore only extend the integration to 2.07 days (three tidal cycles). This simulation is performed for two reasons. The first is to verify convergence with case S, to serve as further evidence (in addition to the observations presented in the next section), that the dynamics captured by our idealized model suite are robust. The second is to uncover additional insights into the submesoscale mixing phenomena arising in the cross-shelf plume regime.

Figure 13 shows surface fields of salinity, freshwater content  $h_f$  and inverse Froude number (as in Figures 3 and 12). We observe the same mechanisms maintaining the cross-shelf plume

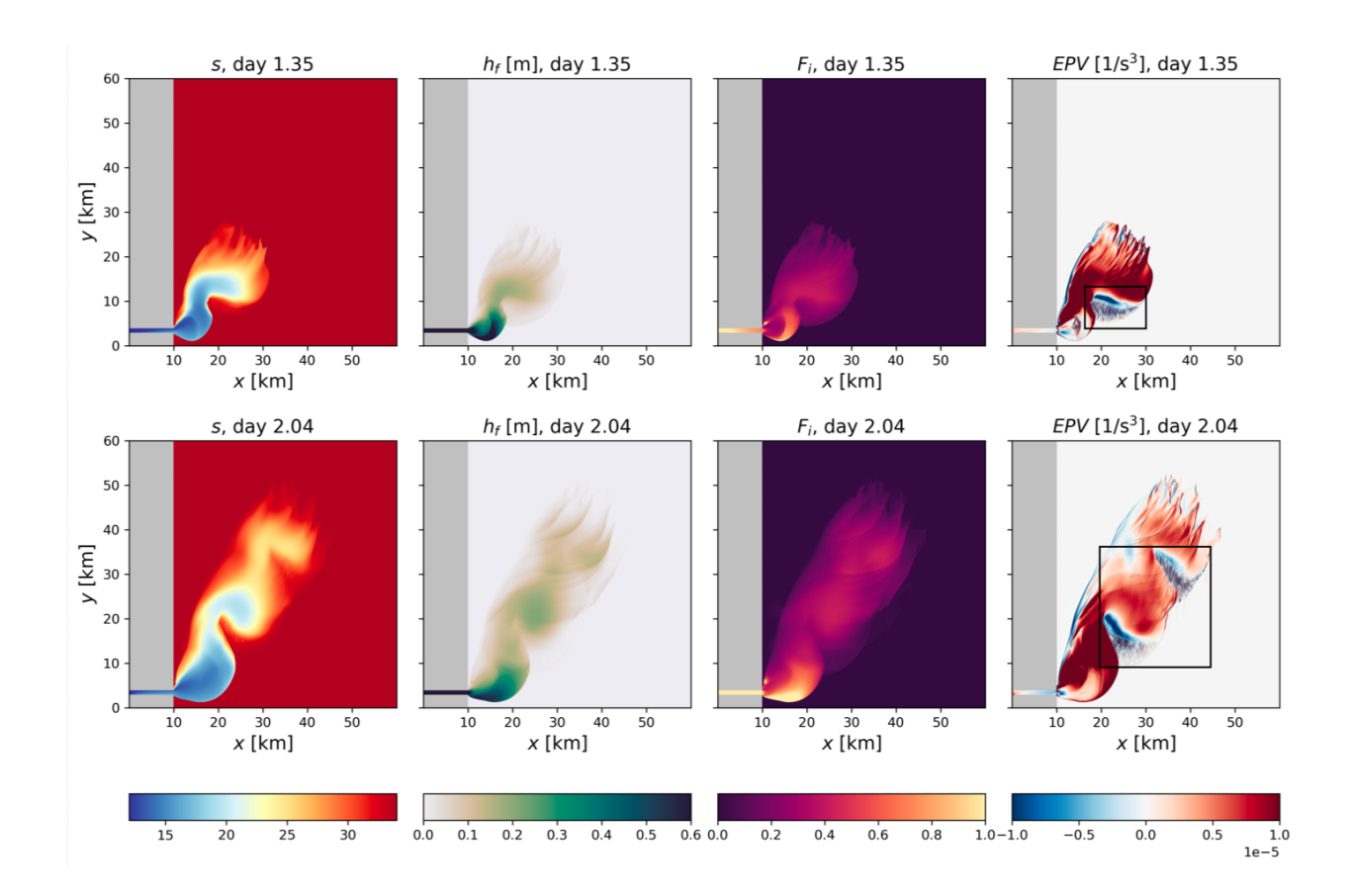


Fig. 13. Case SHR (high-resolution case); note that the domain has been slightly decreased in size to accommodate the higher computational cost. Top row shows fields at 1.35 days, lower row shows fields at 2.07 days (end of simulation). Left to right: surface salinity, equivalent freshwater layer thickness ( $h_f$ ), inverse Froude number ( $F_i < 1$  is supercritical), and Ertel potential vorticity (EPV, with negative values indicating unstable regions). Black rectangles indiciate regions where closeup views will be shown in Figure 14.

regime – solitons radiate from the northern part of the plume and propagate upwind, maintaining its coherence. Here, the solitons are better resolved and disintegrate to form trains of high-frequency internal waves (although we are still unable to resolve the breaking of the internal waves). The distribution and transport of  $h_f$  is very similar to cases S and SNT; compared to Figures 12 and 3 the SHR case even appears to have a higher freshwater layer thickness moving offshore. We also see that the plume maintains supercriticality as in the previously discussed cases. All of these features indicate that our results do converge across resolutions, further validating our model choices.

We now examine the Ertel potential vorticity (Equation 11, Figure 13); as in Section 3a, negative values indicate regions unstable to submesoscale inertial, symmetric, or hybrid inertial-symmetric

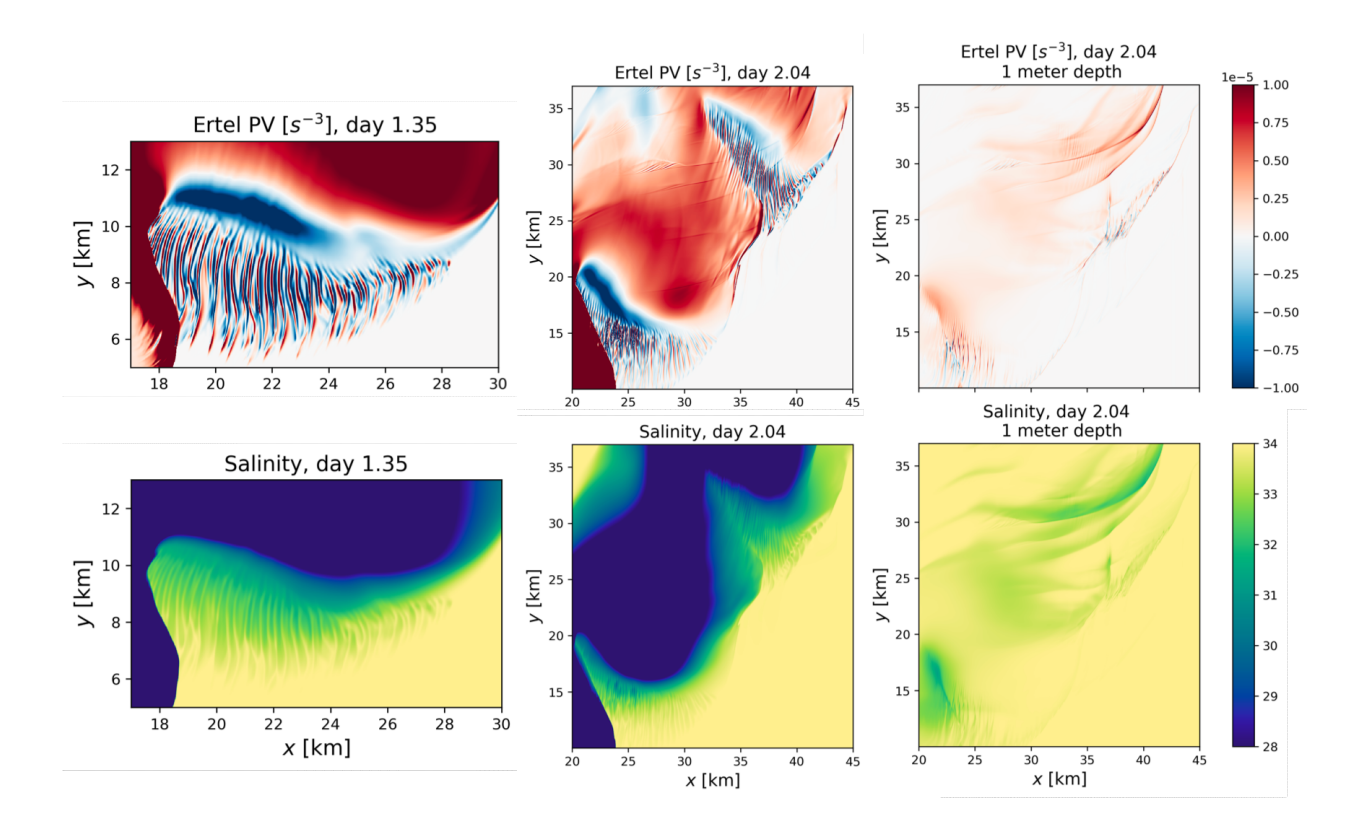


Fig. 14. Closeup views from Figure 13; top row shows Ertel potential vorticity (EPV) and lower row shows salinity. Fields are shown at 1.35 and 2.07 days. The rightmost plots show EPV and salinity at a 1 m depth.

instability (InI, SI, ISI). We observe regions of negative EPV between tidal sub-plumes, along with beam-like structures emanating for several km from the negative EPV regions. As the tidal subplumes propagate into the domain, their boundaries create a sharp density front with the ambient water. Combined with the background geostrophic shear vigorous ISI develops, initiating secondary shear instabilities and mixing. We see contributions both from the lateral and vertical geostrophic shear production terms (Equations 9-10), depending on the evolving orientation of the plume relative to the background geostrophic current. Around 1.35 days, the density front is aligned mostly along the x axis, parallel to  $\partial v_g/\partial x$  and a main energy source is the vertical GSP term (Equation 9). The instability has an SI component at this time (likely coexisting with InI/ISI), with particle displacements mostly parallel to isopycnals. Similar SI dynamics were studied by Yankovsky and Legg (2019) but for the case of a dense shelf plume. We note that in the present scenario the instability dynamics are more complex than much of the theoretical literature on SI due to the background flow field, soliton presence, and rapid advection of the plume front offshore.

Furthermore, the front has a curved structure (rather than two-dimensionally symmetric) and its orientation relative to the background sheared flow changes in space and time. As the plume 561 propagates offshore and the density front changes orientation, the LSP term becomes a dominant 562 energy source, corresponding to hybrid ISI. We show a closeup view in Figure 14; the salinity front is undergoing lateral mixing by the ISI confined to the surface; at a depth of 1 meter we only see a 564 small signature of the ISI-driven mixing and the freshwater penetration is dominated by soliton and 565 internal wave activity. This contrasts with case SNW (Figure 2), where the front is more stationary and thus the instability is able to locally propagate deeper. We emphasize that in this complex 567 scenario, distinguishing SI from hybrid ISI is challenging, and we thus simply conclude that there 568 is a vigorous field of submesoscale instability stemming from the combination of velocity shear 569 (geostrophic and perhaps ageostrophic) and density fronts. Our SHR case is able to resolve frontal 570 ISI motions as well as some of the secondary mixing processes, offering insights into the role of 571 ISI in frontal mixing of a plume. 572

## 5. Discussion

In this study, we have addressed the formation of a cross-shelf buoyant plume by means of 574 idealized numerical experiments. The model reproduces important features of such a plume: the elongated shape of the buoyant layer which detaches from the coast and crosses the shelf curving 576 gradually offshore with distance from the mouth. An important element for the cross-shelf plume 577 is the detachment of the thin buoyant layer from the coast; in this way the discharged water escapes the nearshore regime of overlapping boundary layers and can be advected offshore by 579 the Ekman transport. This can be achieved under light-to-moderate wind conditions when the 580 wind-induced mixing cannot efficiently erode the stratification of the buoyant layer. Once the wind stress increases, surface and bottom boundary layers merge while the rate of alongshore advection increases such that the buoyant water remains trapped nearshore and propagates upstream (i.e., 583 downwind). Even stronger wind allows the offshore spreading of the buoyant water by Ekman 584 dynamics, but in a more conventional, diffuse manner when the along- and cross-shelf scales of the plume become comparable. 586

To further illustrate these two distinct regimes, we present two examples of the Winyah Bay plume. One case, observed on April 26, 2019, represents a typical manifestation of the cross-

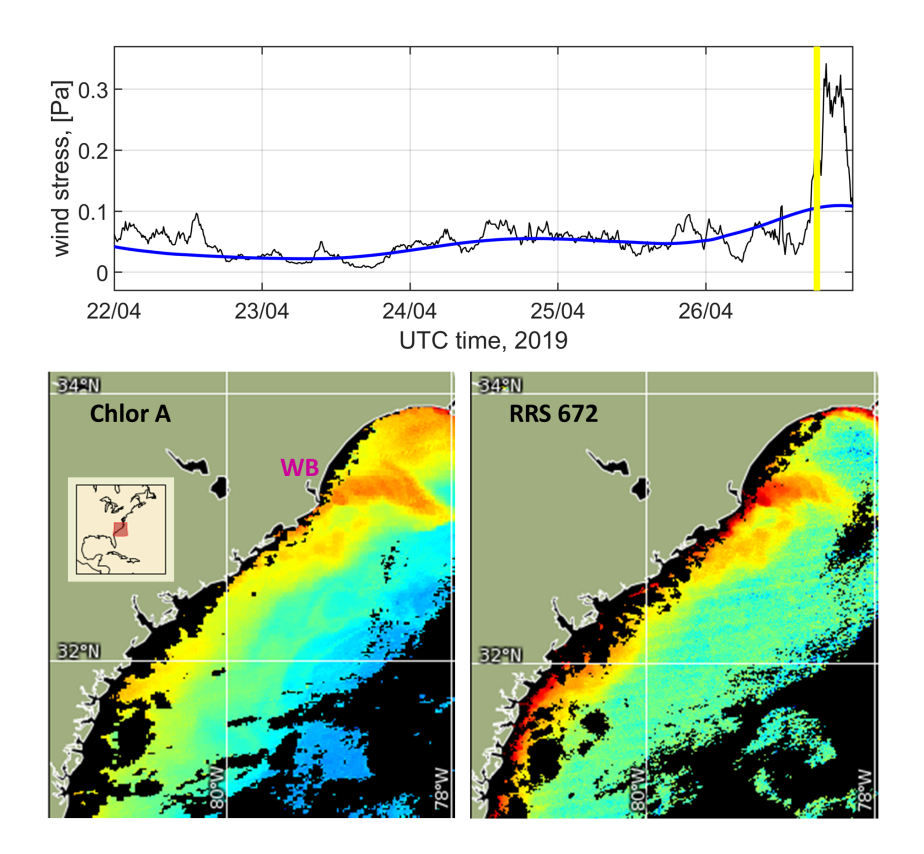


Fig. 15. Cross-shelf WB plume event on April 26, 2019. Top panel: low-pass filtered alongshore wind stress component (heavy line) and instantaneous wind stress magnitude, vertical bar shows time of satellite images; bottom panels: MODIS chlorophyll A from NASA Aqua satellite (left), and VIIRS surface reflectance at 672 nm from NPP satellite (right). Inset shows the location of the study area within the US East Coast. WB is Winyah Bay. Satellite images adapted from NOAA Coastwatch.

shelf plume as described in this paper: an elongated structure detaching from the WB mouth and spreading offshore, crossing almost the entire South Atlantic Bight shelf (Figure 15). Here, the alongshore direction is defined as 40° clockwise from true north. The alongshore low-pass filtered (retaining oscillations longer than 24 h) wind stress component was low, varying within 0.03-0.06 Pa over several days prior to observations, and started to increase just before the images were taken. Since the actual wind is not aligned with the coastline, the instantaneous wind stress magnitude (responsible for mixing) is also shown, and proves that the wind forcing was light to moderate (under 0.1 Pa). We use two proxies for the plume in Figure 15: chlorophyll A measured by a MODIS sensor from the NASA Aqua satellite, and surface reflectance at 672 nm measured by a VIIRS

sensor on a NPP satellite as a proxy for the relative amount of sediments (e.g. Stumpf and Pennock (1989), see also https://coastwatch.noaa.gov/cwn/index.html). These measurements were taken over overlapping time intervals and reveal a similar structure of the WB plume.

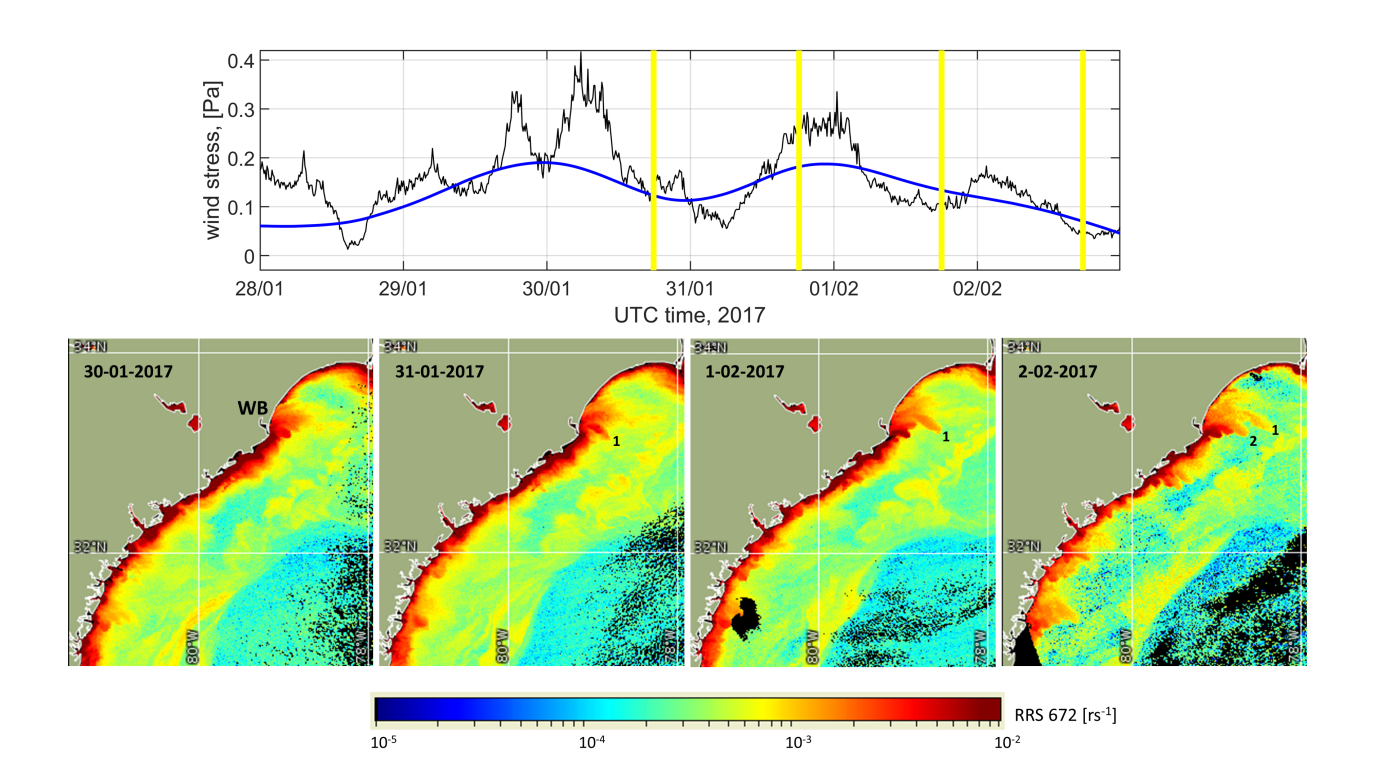


Fig. 16. Cross-shelf plume event on January 30 - February 2, 2017. Same as in Figure 15, except only reflectance at 672 nm is shown at the bottom for four days. Numbers 1 and 2 in satellite images refer to consecutive cross-shelf plumes.

A somewhat different plume structure was observed in late January-early February of 2017 (Figure 16). During this time the wind was also upwelling-favorable, but significantly stronger than in Figure 15: the low-passed alongshore wind stress continuously exceeded 0.1 Pa starting from the beginning of January 29 through the mid-day of February 2. The instantaneous wind stress magnitude on several occasions was in the range of 0.3-0.4 Pa. As a result, the WB plume retained contact with the coastline and the buoyant water was advected both upstream (along the coast) and offshore, similar to the regime in model run V2W10 (i.e., Figures 7d and 8d). This diffusive spreading is the most obvious on 1/30/2017, following the strongest wind forcing.

The wind subsided in the first half of 1/31, so that a tidal sub-plume extending offshore formed (marked with "1" on the satellite image). Once the buoyant water escaped the nearshore trapping, it continued to develop into a filament-like structure, which can be traced in subsequent images. In addition, a second cross-shelf plume comprising several tidal pulses formed by 2/02 (marked with 2) as the low-passed upwelling-favorable wind stress was subsiding over the preceding period of  $\sim 30$  hours. In the event reported in Figure 15, the tidally-averaged freshwater discharge of the Pee Dee River feeding the WB plume was  $\sim 850 \text{ m}^3 \text{ s}^{-1}$  prior to observations, while in the event from Figure 16 the Pee Dee River discharge was lower, ranging within  $450 - 600 \text{ m}^3 \text{ s}^{-1}$ , which could also contribute to more efficient mixing nearshore.

Importantly, the formation of a thin detached buoyant layer (which subsequently evolves into a 626 cross-shelf plume) can occur under a variety of inflow conditions at the mouth: when the Burger 627 number is high (e.g., strong nonlinear momentum advection) or low (e.g., geostrophic adjustment 628 is possible), as well as under steady-state or tidally-modulated inflow. This implies two different 629 mechanisms: hydraulically controlled liftoff due to inherent dynamics of the outflow (high Bu) vs thinning of the buoyant layer under the influence of superimposed wind stress (low Bu). The plume 631 maintains its tight transverse structure due to the radiation of internal solitons from the upstream 632 flank in the upwind (downstream) direction. This radiation is primarily due to the advection of momentum associated with the plume and sustained by the ambient wind-driven circulation. 634 Soliton radiation does not require a tidally-pulsating discharge and can operate when the outflow 635 occurs at a constant rate. However, tidally-modulated discharge makes internal wave radiation more robust because each consecutive tidal pulse produces a corresponding soliton. 637

Light wind forcing conditions imply that the wind stress steers the buoyant layer but cannot produce a sufficiently strong shear stress divergence at its base for ambient water entrainment by means of Kelvin-Helmholtz billows. However, observations reported by Yankovsky and Voulgaris (2019) and Yankovsky et al. (2022) indicate that such a plume does undergo mixing, implying alternative mixing mechanisms. Yankovsky and Voulgaris (2019) proposed that the combination of geostrophic and wind-induced shear within the interior fronts can bring the Richardson number below its critical value. This study points to the role of inertial-symmetric instability in driving plume mixing especially within its frontal areas (which include tidal interior fronts). Since the

638

639

641

642

644

plume remains supercritical, radiating internal solitons can also contribute to mixing, especially as they disintegrate into trains of high frequency internal waves.

While the presented experiments identify important mechanisms affecting the cross-shelf plume farther offshore (beyond its near field), even the high-resolution case is not able to resolve their contribution to frontal dynamics. Traditionally, it is perceived that the far field region is less demanding on spatial resolution (Ralston et al. 2017). However, high frequency internal waves propagating around the offshore rim of the plume or radiating into the upwind front are likely to undergo breaking and generate mixing and entrainment. Frequently observed thermal stratification outside of the plume can also cause some leakage of the internal wave energy outside of the plume, although high frequency internal waves are likely to become evanescent outside of the plume due to the lower buoyancy frequency. Resolving internal wave transformation and dissipation in the plume frontal zone would require a spatial resolution of O(1 m) or even less, and can be addressed in the future either by means of an observational campaign or by LES numerical experiments.

The model configuration in this study is highly idealized, so we briefly address the model limitations. The most obvious simplification is the constant  $A_z$ . However, a more realistic closure scheme can in fact render model results less relevant to observations under the present model configuration. In particular, a closure scheme is likely to predict a stronger eddy viscosity for the unstratified wind-driven flow in the shallow channel so that the bottom boundary layer can easily interact with the plume. Under observed conditions, the surface and bottom boundary layers were separated, in part due to the presence of previously discharged buoyant water, so that the newly discharged wind-driven plume slid on top of the older one (Yankovsky et al. 2022). We maintained this separation in the model by selecting an appropriate value for  $A_z$ , which in fact is close to the observed values in the Winyah Bay plume.

A more subtle but important model artifact is the channel configuration, where the no normal flow boundary condition is applied at the offshore boundary. The free surface does not relax offshore to the unperturbed condition. As a result, the cross-shelf gradient of the alongshore geostrophic velocity is reduced, thus reducing the offshore momentum advection that sustains the soliton radiation. Lastly, periodic boundary conditions imply that there is no alongshore pressure gradient force which typically opposes the wind stress direction (e.g., Carton (1984)). In this case the alongshore velocity is larger (since its acceleration is now balanced by the bottom stress only),

and the plume is likely to be more downwind-swept in our simulations. That is, more realistic open boundary conditions (here, eastern, northern and southern boundaries) would most likely have enhanced the tendency for cross-shelf plume development.

## 6. Conclusions

690

692

693

695

696

We have presented a series of idealized, high-resolution numerical experiments delineating the 680 emergence, dynamics, and parameter space of the newly-identified cross-shelf regime of a river plume. The cross-shelf regime refers to river plumes that propagate offshore, remaining coherent 682 for tens to over one hundred kilometers (as seen in satellite images) away from an estuarine mouth. 683 We first considered a canonical alongshore plume regime in the absence of wind forcing and found that our model captures its well-studied dynamics. The plume undergoes geostrophic adjustment, 685 forming a mid-field buoyant bulge and a far-field coastal current that propagates alongside the 686 shelf. A new result from this case was the presence of inertial-symmetric instability (ISI) within 687 the plume. We were able to resolve beams of ISI leading to deepening of the plume front and lateral mixing. 689

We then incorporated an upwelling-favorable wind forcing into our model and observed the emergence of the cross-shelf regime. The plume detaches from the coast in a thin buoyant layer that then propagates tens of kilometers offshore. Remarkably, the plume remains highly coherent, with its width not increasing substantially with distance from the mouth. The coherence is attributed to radiation of internal solitons in the offshore part of the plume which propagate from upstream to downstream (upwind) flank of the plume. The solitons carry mass and momentum within the plume and suppress diffusive spreading and widening of the plume with distance offshore.

We considered the parameter space over which the cross-shelf plume regime arises by introducing tidally-modulated buoyant inflow, varying the river mouth width (causing the Burger number to change), changing wind forcing magnitude, and testing the influence of a different coastal geometry (a promontory). We find that the regime is robust and may come about through various scenarios. These include: low Bu (wide mouth), high Bu (narrow mouth), steady-state inflows, tidally-modulated inflows, different coastal geometries, and light to moderate upwelling-favorable wind stress. We find that the regime breaks down under high wind forcing conditions when the formation of the thin, detached buoyant layer is suppressed by vertical mixing.

We additionally presented an ultra-high resolution case (SHR) analogous to our standard case 705 with tidal forcing (S). The dynamics in SHR were consistent with S, albeit permitting the additional 706 resolution of internal wave trains evolving from solitons. The convergence between S and SHR 707 further validated our model setup. In SHR the horizontal resolution was 15 m, allowing us to resolve submesoscale instability dynamics. We observed the presence of large regions of negative 709 Ertel potential vorticity (EPV) at fronts generated between tidal sub-plumes. Vigorous ISI develops 710 out of the negative EPV regions and is seen as alternating beams between the plume fronts. The 711 ISI causes lateral tracer mixing and frontal erosion at the surface, while internal waves and solitons initiate mixing and freshwater penetration vertically. 713

Finally, we looked at observations of the Winyah Bay plume. As predicted by our model, we observe the cross-shelf regime under favorable wind forcing conditions. Overall, the cross-shelf 715 plume appears to be a robust and efficient mechanism for cross-shelf exchange, especially for wide 716 continental shelves affected by significant freshwater discharge. It can be formed on timescales 717 of just a few days, much faster than the classical anticyclonic bulge, and the required forcing conditions are fairly typical, at least for the US East Coast. As a transient feature with a transverse 719 horizontal scale of O(10 km) and depth of just a few meters, cross-shelf plumes are unlikely to be 720 resolved by general circulation or climate models. Hence, their impact on the cross-shelf transport of freshwater with associated suspended and dissolved material of terrigenous origin needs to be 722 parameterized in such models.

- Acknowledgments. AY was supported by the NSF grant OCE-2148480. We are indebted to
- George Marmorino and two anonymous reviewers for their insightful comments and suggestions.
- Data availability statement. Observational data are available at the following websites. Satellite
- images: https://coastwatch.chesapeakebay.noaa.gov/region\_cl.php; buoy wind data:
- https://www.ndbc.noaa.gov/; and freshwater discharge: https://waterdata.usgs.gov/
- nwis/. Model data for simulations presented in this study are available upon request. Codes
- for analysis and figure generation may be accessed at https://doi.org/10.5281/zenodo.
- 731 7557654.

### 732 References

- Apel, J. R., L. A. Ostrovsky, Y. A. Stepanyants, and J. F. Lynch, 2007: Internal solitons in the ocean and their effect on underwater sound. *The Journal of the Acoustical Society of America*, 121 (2), 695–722, https://doi.org/10.1121/1.2395914.
- Arneborg, L., V. Fiekas, L. Umlauf, and H. Burchard, 2007: Gravity current dynamics and entrainment a process study based on observations in the Arkona Basin. *Journal of Physical Oceanography*, **37** (8), 2094–2113, https://doi.org/10.1175/JPO3110.1, publisher: American Meteorological Society Section: Journal of Physical Oceanography.
- Ayouche, A., X. Carton, G. Charria, S. Theettens, and N. Ayoub, 2020: Instabilities and vertical mixing in river plumes: application to the Bay of Biscay. *Geophysical & Astrophysical Fluid Dynamics*, **114** (**4-5**), 650–689, https://doi.org/10.1080/03091929.2020.1814275.
- Ayouche, A., G. Charria, X. Carton, N. Ayoub, and S. Theetten, 2021: Non-linear processes in the
  Gironde river plume (north-east Atlantic): instabilities and mixing. *Frontiers in Marine Science*,

  8.
- Bachman, S. D., B. Fox-Kemper, J. R. Taylor, and L. N. Thomas, 2017: Parameterization of frontal symmetric instabilities. I: Theory for resolved fronts. *Ocean Modelling*, **109**, 72–95, https://doi.org/10.1016/j.ocemod.2016.12.003.
- Branch, R. A., A. R. Horner-Devine, N. Kumar, and A. R. Poggioli, 2020: River Plume Liftoff
   Dynamics and Surface Expressions. *Water Resources Research*, 56 (7), https://doi.org/10.1029/
   2019WR026475.

- Brink, K. H., 2016: Cross-shelf exchange. *Annual Review of Marine Science*, **8** (**1**), 59–78, https://doi.org/10.1146/annurev-marine-010814-015717.
- Carton, J. A., 1984: Coastal Circulation Caused by an Isolated Storm. *Journal of Physical Oceanog*raphy, **14** (1), 114–124, https://doi.org/10.1175/1520-0485(1984)014\dagger 0114:CCCBAI\dagger 2.0.CO;
- Chao, S.-Y., and W. C. Boicourt, 1986: Onset of estuarine plumes. *Journal of Physical Oceanogra*phy, **16 (12)**, 2137–2149, https://doi.org/10.1175/1520-0485(1986)016\( 2137:OOEP\) 2.0.CO; 2.
- Delatolas, N., D. G. MacDonald, L. Goodman, M. Whitney, K. Huguenard, and K. Cole, 2023:

  Comparison of structure and turbulent mixing between lateral and leading-edge river plume
  fronts: Microstructure observations from a T-REMUS AUV. *Estuarine*, *Coastal and Shelf*Science, 283, 108 234, https://doi.org/10.1016/j.ecss.2023.108234.
- Garvine, R. W., 1984: Radial spreading of buoyant, surface plumes in coastal waters.

  Journal of Geophysical Research: Oceans, 89 (C2), 1989–1996, https://doi.org/10.1029/

  JC089iC02p01989.
- Garvine, R. W., 1987: Estuary plumes and fronts in shelf waters: a layer model. *Journal of Physical Oceanography*, **17** (11), 1877–1896, https://doi.org/10.1175/1520-0485(1987)017\langle 1877: EPAFIS\rangle 2.0.CO;2.
- Geyer, W. R., and D. K. Ralston, 2011: 2.03 The dynamics of strongly stratified estuaries. *Treatise on Estuarine and Coastal Science*, Academic Press, 37–51, https://doi.org/10.1016/
  B978-0-12-374711-2.00206-0.
- Grisouard, N., 2018: Extraction of potential energy from geostrophic fronts by inertial—symmetric instabilities. *Journal of Physical Oceanography*, 48 (5), 1033–1051, https://doi.org/10.1175/
   JPO-D-17-0160.1, publisher: American Meteorological Society Section: Journal of Physical Oceanography.
- Hetland, R. D., 2005: Relating river plume structure to vertical mixing. *Journal of Physical Oceanography*, **35** (9), 1667–1688, https://doi.org/10.1175/JPO2774.1, publisher: American Meteorological Society Section: Journal of Physical Oceanography.

- Hetland, R. D., 2010: The effects of mixing and spreading on density in near-field river plumes.
- Dynamics of Atmospheres and Oceans, 49 (1), 37–53, https://doi.org/10.1016/j.dynatmoce.2008.
- 781 11.003.
- Hickey, B., R. McCabe, S. Geier, E. Dever, and N. Kachel, 2009: Three interacting freshwater
- plumes in the northern California Current System. Journal of Geophysical Research: Oceans,
- <sup>784</sup> **114 (C2)**, https://doi.org/10.1029/2008JC004907.
- Horner-Devine, A. R., R. D. Hetland, and D. G. MacDonald, 2015: Mixing and transport in
- coastal river plumes. Annual Review of Fluid Mechanics, 47 (1), 569–594, https://doi.org/
- <sup>787</sup> 10.1146/annurev-fluid-010313-141408.
- Hoskins, B. J., 1974: The role of potential vorticity in symmetric stability and instability. *Quarterly*
- Journal of the Royal Meteorological Society, **100** (425), 480–482, https://doi.org/10.1002/qj.
- 49710042520.
- <sup>791</sup> Igeta, Y., A. Yankovsky, K.-i. Fukudome, S. Ikeda, N. Okei, K. Ayukawa, A. Kaneda, and
- T. Watanabe, 2017: Transition of the Tsushima Warm Current path observed over Toyama
- Trough, Japan. Journal of Physical Oceanography, 47 (11), 2721–2739, https://doi.org/
- <sup>794</sup> 10.1175/JPO-D-17-0027.1.
- <sup>795</sup> Izett, J. G., and K. Fennel, 2018: Estimating the cross-shelf export of riverine materials: Part 1.
- general relationships from an idealized numerical model. Global Biogeochemical Cycles, 32 (2),
- <sup>797</sup> 160–175, https://doi.org/10.1002/2017GB005667.
- <sub>798</sub> Jia, Y., and A. Yankovsky, 2012: The impact of ambient stratification on freshwater transport in a
- river plume. *Journal of Marine Research*, **70**, https://doi.org/10.1357/002224012800502408.
- Lentz, S. J., 2001: The influence of stratification on the wind-driven cross-shelf circulation over
- the North Carolina shelf. Journal of Physical Oceanography, 31 (9), 2749–2760, https://doi.org/
- 802 10.1175/1520-0485(2001)031\(\rangle 2749:TIOSOT\\rangle 2.0.CO; 2.
- Lv, R., P. Cheng, and J. Gan, 2020: Adjustment of river plume fronts during downwelling-
- favorable wind events. Continental Shelf Research, 202, 104 143, https://doi.org/10.1016/j.csr.
- 805 2020.104143.

- MacDonald, D. G., and W. R. Geyer, 2005: Hydraulic control of a highly stratified estuarine
- front. Journal of Physical Oceanography, **35** (**3**), 374–387, https://doi.org/10.1175/JPO-2692.1,
- publisher: American Meteorological Society Section: Journal of Physical Oceanography.
- Marshall, J., A. Adcroft, C. Hill, L. Perelman, and C. Heisey, 1997: A finite-volume, incompressible
- Navier Stokes model for studies of the ocean on parallel computers. *Journal of Geophysical*
- Research: Oceans, **102** (**C3**), 5753–5766, https://doi.org/10.1029/96JC02775.
- McDougall, T. J., D. R. Jackett, D. G. Wright, and R. Feistel, 2003: Accurate and computationally
- efficient algorithms for potential temperature and density of seawater. *Journal of Atmospheric*
- and Oceanic Technology, **20** (5), 730–741, https://doi.org/10.1175/1520-0426(2003)20\(\gamma\)730:
- 815 AACEAF \ 2.0.CO; 2.
- Nof, D., and T. Pichevin, 2001: The Ballooning of Outflows. Journal of Physical Oceanogra-
- phy, **31** (**10**), 3045–3058, https://doi.org/10.1175/1520-0485(2001)031(3045:TBOO)2.0.CO;2,
- publisher: American Meteorological Society Section: Journal of Physical Oceanography.
- O'Donnell, J., 1990: The formation and fate of a river plume: a numerical model. Journal of
- Physical Oceanography, **20** (**4**), 551–569, https://doi.org/10.1175/1520-0485(1990)020(0551:
- 821 TFAFOA \ \ 2.0.CO; 2.
- O'Donnell, J., 2010: The dynamics of estuary plumes and fronts. Contemporary Issues in Es-
- tuarine Physics, A. Valle-Levinson, Ed., Cambridge University Press, Cambridge, 186–246,
- https://doi.org/10.1017/CBO9780511676567.009.
- Oey, L.-Y., and G. L. Mellor, 1993: Subtidal variability of estuarine outflow, plume, and coastal
- current: a model study. Journal of Physical Oceanography, 23 (1), 164–171, https://doi.org/
- 10.1175/1520-0485(1993)023(0164:SVOEOP)2.0.CO;2, publisher: American Meteorological
- Society Section: Journal of Physical Oceanography.
- Ralston, D. K., G. W. Cowles, W. R. Geyer, and R. C. Holleman, 2017: Turbulent and numerical
- mixing in a salt wedge estuary: Dependence on grid resolution, bottom roughness, and turbulence
- closure. Journal of Geophysical Research: Oceans, 122 (1), 692–712, https://doi.org/10.1002/
- 832 2016JC011738.

- Sharples, J., J. J. Middelburg, K. Fennel, and T. D. Jickells, 2017: What proportion of riverine nutrients reaches the open ocean? *Global Biogeochemical Cycles*, **31** (1), 39–58, https://doi.org/
- Stumpf, R. P., and J. R. Pennock, 1989: Calibration of a general optical equation for remote sensing of suspended sediments in a moderately turbid estuary. *Journal of Geophysical Research:*Oceans, 94 (C10), 14 363–14 371, https://doi.org/10.1029/JC094iC10p14363.
- Thomas, L. N., J. R. Taylor, R. Ferrari, and T. M. Joyce, 2013: Symmetric instability in the Gulf

  Stream. *Deep Sea Research Part II: Topical Studies in Oceanography*, **91**, 96–110, https://doi.org/

  10.1016/j.dsr2.2013.02.025.
- Wenegrat, J. O., and L. N. Thomas, 2020: Centrifugal and symmetric instability during Ekman
   adjustment of the bottom boundary layer. *Journal of Physical Oceanography*, **50** (6), 1793–1812,
   https://doi.org/10.1175/JPO-D-20-0027.1.
- Whitney, M. M., 2023: Separation of the Icelandic Coastal Current from the Reykjanes Peninsula.

  Estuarine, Coastal and Shelf Science, 280, 108 163, https://doi.org/10.1016/j.ecss.2022.108163.
- Yankovsky, A. E., and D. C. Chapman, 1997: A simple theory for the fate of buoyant coastal discharges. *Journal of Physical Oceanography*, **27** (7), 1386–1401, https://doi.org/10.1175/ 1520-0485(1997)027\langle1386:ASTFTF\rangle2.0.CO;2, publisher: American Meteorological Society Section: Journal of Physical Oceanography.
- Yankovsky, A. E., D. B. Fribance, D. Cahl, and G. Voulgaris, 2022: Offshore spreading of a supercritical plume under upwelling wind forcing: a case study of the Winyah Bay outflow.

  Frontiers in Marine Science, 8.
- Yankovsky, A. E., and G. Voulgaris, 2019: Response of a coastal plume formed by tidally modulated estuarine outflow to light upwelling-favorable wind. *Journal of Physical Oceanography*, **49** (3), 691–703, https://doi.org/10.1175/JPO-D-18-0126.1.
- Yankovsky, E., and S. Legg, 2019: Symmetric and baroclinic in dense shelf overflows. *Journal*of Physical Oceanography, **49** (**1**), 39–61, https://doi.org/10.1175/JPO-D-18-0072.1, publisher:
  American Meteorological Society.

- 260 Zhou, S., and H. Wu, 2023: Cross-shelf penetrating fronts of buoyant coastal currents around the
- headland. Journal of Geophysical Research: Oceans, 128 (5), e2022JC019 371, https://doi.org/
- 10.1029/2022JC019371.